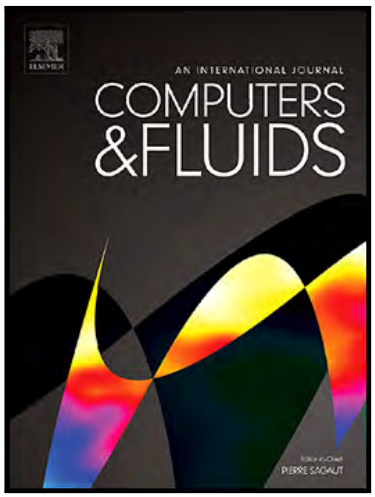

A 1D numerical model for the simulation of unsteady and highly erosive flows in rivers

S. Martínez-Aranda, J. Murillo, P. García-Navarro

PII: S0045-7930(19)30009-X
DOI: https://doi.org/10.1016/j.compfluid.2019.01.011
Reference: CAF 4099

To appear in: *Computers and Fluids*

Received date: 19 February 2018
Revised date: 14 November 2018
Accepted date: 8 January 2019

Please cite this article as: S. Martínez-Aranda, J. Murillo, P. García-Navarro, A 1D numerical model for the simulation of unsteady and highly erosive flows in rivers, *Computers and Fluids* (2019), doi: https://doi.org/10.1016/j.compfluid.2019.01.011

Highlights

- Coupled Roe's scheme for SW-Exner equations in cross-section averaged erosive flows.
- Explicit expressions for eigenvalues, eigenvectors, wave and source strengths.
- A new parameter c_b related to the bed change appears in the coupled Jacobian matrix.
- c_b depends on the erosion-deposition mechanism selected to update the cross-section.
- Analytical expression for the equilibrium bed slope in variable width rectangular channels.

A 1D numerical model for the simulation of unsteady and highly erosive flows in rivers

S. Martínez-Aranda*, J. Murillo, P. García-Navarro

LIFTEC-CSIC, University of Zaragoza, Spain

Abstract

This work is focused on a numerical finite volume scheme for the coupled shallow water-Exner system in 1D applications with arbitrary geometry. The mathematical expressions modeling the hydrodynamic and morphodynamic components of the physical phenomenon are treated to deal with cross-section shape variations and empirical solid discharge estimations. The resulting coupled equations can be rewritten as a non-conservative hyperbolic system with three moving waves and one stationary wave to account for the source terms discretization. Moreover, the wave celerities for the coupled morpho-hydrodyamical system depend on the erosion-deposition mechanism selected to update the channel cross-section profile. This influence is incorporated into the system solution by means of a new parameter related to the channel bottom variation celerity. Special interest is put to show that, even for the simplest solid transport models as the Grass law, to find a linearized Jacobian matrix of the system can be a challenge in presence of arbitrary shape channels. In this paper a numerical finite volume scheme is proposed, based on an augmented Roe solver, first order accurate in time and space, dealing with solid transport flux variations caused by the channel geometry changes. Channel cross-section variations lead to the appearance of a new solid flux source term which should be discretized properly. The stability region is controlled by wave celerities together with a proper reconstruction of the approximate local Riemann problem solution, enforcing positive values for the intermediate states of the conserved variables. Comparison of the numerical results for several analytical and experimental cases demonstrates the effectiveness, exact well-balancedness and accuracy of the scheme.

*Corresponding author: sermar@unizar.es

Keywords:
Finite volume method, shallow water equations, Exner equation, coupled method, augmented Roe's scheme, variable geometry

1. Introduction

Sediment transport processes in rivers are broadly classified into two different types, bed load movement and suspended material transport, and they are basically caused by the gravity and friction forces at the river bed level [1]. Bed load transport takes into account the sediment movements that occur without the solid grain losing contact with the river bed (rolling, sliding and saltation motion mechanisms), whereas suspension transport considers both the solid mass which is transported by the flow as a solute. Both transport processes occur simultaneously and to identify a threshold between them is an open research topic. Sediment transport processes are usually modelled by means of a set of equations which includes hydrodynamic and morphodynamic components. The hydrodynamic part can be described by the shallow water equations (SW), commonly used to study water movements in rivers and channels. On the other hand, the morphodynamical component is commonly represented by a system of equations modelling the solid mass conservation property.

The relation between the actual solid transport flux and the flow dynamic features has become one of the major uncertainty sources for sediment transport modellers. The traditional approach is based on the assumption that the actual solid transport rate adapts immediately to the hydrodynamic properties (capacity or equilibrium approach). Sediment transport capacity can be understood as the maximum amount of sediment that can be transported by a flow in a particular steady state. Models based on this assumption have been proposed to compute many experimental and real-scale sediment transport problems [2–6]. Nevertheless, in the two last decades, a new approach accounting for the time and space lag between the actual solid fluxes and the local hydrodynamic properties has received increasing attention [7]. Non-capacity or non-equilibrium models have been reported by many authors [8–13] for both bed load and suspended load sediment transport processes. Although physically the non-capacity assumption seems to be always justified, especially when dealing with highly erosive and unsteady flows, capacity models have demonstrated to be applicable for bed load transport processes in uniform sediment beds and high-magnitude flow conditions [10, 11, 14, 15].

The capacity assumption for the bed load sediment transport leads to reductions on both the number of equations involved (four and three equations for 1D non-capacity and capacity models, respectively) and on the number of closure relations (adaptation lenght and net solid flux between active and non-active sediment layers are not necessary). Capacity models formulate the solid mass conservation by means of the well-known Exner equation [16] and only need a closure relation for the capacity transport rate. Different empirical equations can be found in literature to determine the bed-load transport capacity (see [17] for a brief summary), being this one of the major uncertainty sources for equilibrium models. In most of them, the sediment movement is controlled by the critical shear stress, a physical parameter which is experimentally determined. The reduction on the number of equations and closure relations implies a decreased computational cost for capacity bed load models, allowing a better efficiency in long-term real-scale cases.

Two-dimensional models have been commonly reported to simulate flow and sediment transport, together with a fine representation of topography and local hydraulic effects [6, 18, 19]. However, their application to real river cases is still restricted due to the computational time required and the amount of field data needed for the model calibration. Therefore, two-dimensional models have been mainly applied to reach-scale domain cases with short event time duration. However, the latest improvements in their computational efficiency thanks to the use of GPU implementation [20] or local-time-step approach [21] are widening the applicability of 2D models. On the other hand, one-dimensional models require less field data and offer a higher computational efficiency. Although 1D models are not able to capture all the complex two-dimensional features of an unsteady flow in arbitrary topographies, they may become a useful tool for engineers in order to predict flood episodes and their consequences, where computation time is a key factor in order to avoid material damages and human losses.

The hydrodynamic and morphodynamic equations that describe the bed-load transport phenomena constitute a coupled system of conservation laws. Although the numerical modeling of free-surface flows with bed evolution involves transient water flow and movable bed boundaries, decoupled methods have been commonly reported to evaluate the bed morphodynamics in 1D realistic application [22–25]. In these works, shallow water and sediment equations are independently solved. The decoupling approaches have been successfully applied to test cases with weak interactions and slow geometrical evolutions. However, when the two physical components of the system have

relatively strong interactions, the decoupling strategy can create spurious oscillations [26].

Coupling bed-load transport into the hydrodynamic shallow water system is a more challenging topic since it leads to a more complicated eigenstructure. From a mathematical point of view, coupling the morphodynamic model with SW equations allows us to apply a stable hyperbolic solver with a dynamic time step based on a CFL stability condition in order to avoid nonphysical oscillations and deal with geometrical discontinuities potentially formed during the bed evolution process. So far, coupled models reported in literature were only developed for unit-width formulations, hindering their application to complex 1D geometry models [4, 5, 27–31]. Therefore, a numerical 1D coupled model able to simulate complex geometries efficiently and demonstrate its performance in realistic applications is still required.

In [32] a capacity Exner-based coupled model for two-dimensional transient flows over erodible beds on triangular unstructured meshes was proposed using a special coupling strategy to incorporate the bed slope source term to the flux Jacobian matrix. This efficient method was later used by [18, 33] to develop numerical schemes for the SW-Exner coupled system. In the present work, this procedure is extended to incorporate the bed slope component to the cross-section averaged fluxes for a one-dimensional model, allowing to develop a coupled scheme based on the Augmented Roe's solver which is able to deal with non prismatic channels, preserving the solid mass conservation property and the stability region.

This paper is structured as follows: In Section 2 the governing equations are presented, identifying clearly flux variations and source terms only depending on the geometrical changes. The resulting system allows us to write a numerical scheme able to handle variable cross-sections, which is described in Section 3. In this section we also report proper numerical fixes to deal with non-movable bed conditions and to ensure not excessive time step reductions. A set of analytical, experimental and real-scale field tests are used to compare with the numerical results in Section 4, in order to report the model capability to handle cross-section changes. The performance in non-movable bed conditions and their accuracy using different empirical closure formulae for the solid discharge are also evaluated. Finally, conclusions are highlighted in Section 5. Additionally, explicit expressions for wave and source terms strengths needed to complete the numerical scheme, and an analytical solution for erosive steady state in a variable-width rectangular channel are reported in the appendix sections.

2. Mathematical model

2.1. Governing equations

Free-surface flow movement in one-dimensional practical applications, considering a complex cross-sectional shape channel, can be modeled by the Saint-Venant equations for the mass and momentum conservation [34]. The temporal evolution of the conserved flow variables depends on the spatial variation of the hydrodynamic fluxes as follows:

$$\frac{\partial A}{\partial t} + \frac{dQ}{dx} = 0 \tag{1}$$

$$\frac{\partial Q}{\partial t} + \frac{d}{dx}\left(\frac{Q^2}{A} + gI_1\right) = g\left(I_2 + AS_0 - AS_f\right) \tag{2}$$

where $A(x,t)$ is the wetted cross-sectional area, $Q(x,t)$ is the flow discharge, g is the acceleration of gravity, S_0 is the bed slope and S_f is the friction slope. I_1 represents the hydrostatic pressure force term in a section of maximum water depth h and I_2 accounts for the pressure force due to longitudinal variations of the channel width $\sigma(x,\eta)$ (Fig. 1):

$$A(x,t) = \int_0^{h(x,A)} \sigma(x,\eta)\ d\eta$$

$$I_1(x,A) = \int_0^{h(x,A)} \left(h(x,A) - \eta\right)\sigma(x,\eta)\ d\eta$$

$$I_2(x,A) = \int_0^{h(x,A)} \left(h(x,A) - \eta\right)\frac{\partial \sigma(x,\eta)}{\partial x}\ d\eta$$

The above equations can be also written in vector form as:

$$\frac{\partial \vec{V}}{\partial t} + \frac{d\vec{F}(x,\vec{V})}{dx} = \vec{R}(x,\vec{V}) \tag{3}$$

being $\vec{V}$ the conserved variables, $\vec{F}$ the conservative fluxes vector and $\vec{R}$ the vector accounting for the source terms. Note that the consideration of domains with complex tophography, such as rivers, leads to the total spatial variation of the cross-section averaged fluxes involved in Saint-Venant equations cannot be directly expressed only in terms of conserved variables derivatives as they also depend on the geometrical changes in the domain,

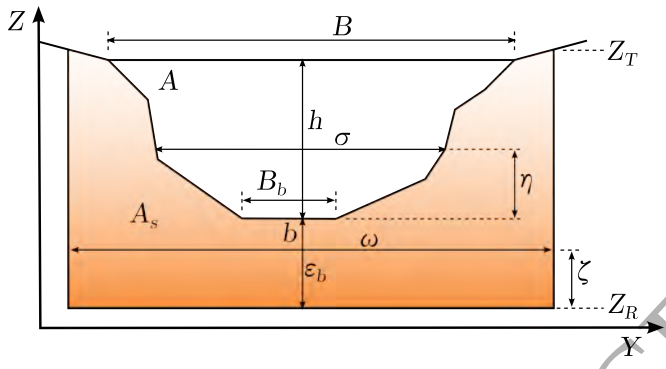

Figure 1: Arbitrary cross-section geometrical description.

that is $\vec{F} = \vec{F}(x, \vec{V})$. This issue could lead to problems in order to design an efficient numerical scheme which represents the conservative fluxes by means of a Jacobian matrix defined as the partial derivative of the fluxes respect to the flow variables [35]. Focusing on the momentum equation and using Leibnitz's rule, it is possible to find an expression for the total spatial derivative of I_1 in which variations depending purely on the cross-sectional geometry ($A = const$) are separated from the component only related to the conserved flow variables ($x = const$) [35–37].

$$\frac{dI_1}{dx} = \left.\frac{\partial I_1}{\partial x}\right|_{A=const} + \left.\frac{\partial I_1}{\partial A}\frac{\partial A}{\partial x}\right|_{x=const} = \left(I_2 + A\frac{\partial h}{\partial x}\right) + \frac{A}{B}\frac{dA}{dx} \tag{4}$$

being $B(x, A)$ the channel width at the water surface. Replacing (4) in (2):

$$\frac{\partial Q}{\partial t} + \frac{d}{dx}\left(\frac{Q^2}{A}\right) + g\frac{A}{B}\frac{dA}{dx} = gAS_0 - gAS_f - gA\frac{\partial h}{\partial x} \tag{5}$$

The new conservative flux on the left side of (5) depends on the conserved variables exclusively, avoiding the numerical computation of I_1 and I_2 additionaly.

Finally, it is important to stress that the discrete increments $\delta/\delta x$ of the function h required by the numerical scheme actually approach the total derivative instead of the partial derivative $\partial h/\partial x$. For this reason partial derivatives should be avoided in the mathematical formulation leading to the numerical discretization [36]. From $h = h(x, A)$:

$$\frac{dh}{dx} = \left.\frac{\partial h}{\partial x}\right|_{A=const} + \left.\frac{\partial h}{\partial A}\frac{\partial A}{\partial x}\right|_{x=const} = \frac{\partial h}{\partial x} + \frac{1}{B}\frac{dA}{dx} \tag{6}$$

Therefore, replacing the partial derivative $\partial h/\partial x$ in (5) by its expression deduced from (6), the second hydrodynamic conservation law could be expressed in terms of total derivatives as follows:

$$\frac{\partial Q}{\partial t} + \frac{d}{dx}\left(\frac{Q^2}{A}\right) + g\frac{A}{B}\frac{dA}{dx} = gAS_0 - gAS_f - gA\left(\frac{dh}{dx} - \frac{1}{B}\frac{dA}{dx}\right) \quad (7)$$

Note that this formulation does not include the hydrostatic pressure integrals any more, so it is no longer necessary to compute them. The presence of the bottom force gAS_0, which can lead to inaccurate evaluations of the pressure force in sections with very irregular shapes over steep slopes [38], is balanced here by the new term $gA(\frac{dh}{dx} - \frac{1}{B}\frac{dA}{dx})$, that has been carefully formulated to avoid partial derivatives [35, 37]. Therefore, thanks to the above algebraic manipulations, the resulting formulation is as robust as the ones reported in [39] or [38], where computation of I_1 and I_2 was included. It is worth to note that the computation of the pressure integrals can be a difficult task in very irregular geometries, hence this formulation improves the computational efficiency of the model without causes inaccurate evaluations of the integral force in complex cross-sections.

On the other hand, bed-load mass conservation is modelled here by means of the Exner continuity equation [16], which has the following expression for an arbitrary channel cross-section:

$$\frac{\partial A_s}{\partial t} + \xi\frac{dQ_s(x, A, Q)}{dx} = 0 \quad (8)$$

where $A_s(x,t)$ is the solid area, $Q_s(x, A, Q)$ the total solid discharge at the cross-section and $\xi = 1/(1-p)$, being p the bed load layer porosity. A_b and Q_s are defined as:

$$\begin{aligned} A_s(x,t) &= \int_0^{Z_T(x)-Z_R(x)} \left[\omega(x,\zeta) - \sigma(x,\zeta)\right]\, d\zeta \\ Q_s(x,A,Q) &= \int_0^{B(x,A)} q_s(A,Q)\, dy \end{aligned} \quad (9)$$

where $q_s(A,Q)$ is the solid discharge per unit width and $\omega(x,\zeta)$ is the erodible domain width. As a first hypothesis, the total bed load discharge can be defined considering a constant bed load transport rate per unit width applied to the whole cross-section [25, 40].

$$Q_s(x, A, Q) = B(x, A)\ q_s(A, Q) \tag{10}$$

Note again that the total derivative of the total sediment solid discharge at the channel cross-section $Q_s(x, A, Q)$ can be written in the following way:

$$\frac{dQ_s(x, A, Q)}{dx} = \left.\frac{\partial Q_s}{\partial x}\right|_{A,Q=const} + \left.\frac{\partial Q_s}{\partial A}\frac{\partial A}{\partial x}\right|_{x,Q=const} + \left.\frac{\partial Q_s}{\partial Q}\frac{\partial Q}{\partial x}\right|_{x,A=const} \tag{11}$$

Therefore, from (10), the partial derivatives in (11) are expressed as:

$$\begin{aligned}
\frac{\partial Q_s(x, A, Q)}{\partial x} &= \frac{\partial B(x, A)}{\partial x}\ q_s(A, Q) \\
\frac{\partial Q_s(x, A, Q)}{\partial A} &= \frac{\partial B(x, A)}{\partial A}\ q_s(A, Q) + B(x, A)\frac{\partial q_s(A, Q)}{\partial A} \\
\frac{\partial Q_s(x, A, Q)}{\partial Q} &= B(x, A)\frac{\partial q_s(A, Q)}{\partial Q}
\end{aligned} \tag{12}$$

Replacing (12) in (11) and reordering terms, an expression for the total derivative of the solid discharge, which could be used in arbitrary cross-section channels, can be obtained.

$$\begin{aligned}
\frac{dQ_s}{dx} &= \left(\frac{\partial B}{\partial x} + \frac{\partial B}{\partial A}\frac{\partial A}{\partial x}\right) q_s + B\frac{\partial q_s}{\partial A}\frac{\partial A}{\partial x} + B\frac{\partial q_s}{\partial Q}\frac{\partial Q}{\partial x} = \\
&= \frac{dB}{dx} q_s + B\frac{\partial q_s}{\partial A}\frac{dA}{dx} + B\frac{\partial q_s}{\partial Q}\frac{dQ}{dx}
\end{aligned} \tag{13}$$

Taking into account (13), the Exner continuity equation can be written so that the conservative solid flux only depends on the conserved flow variables. Furthermore, a new source term appears which represents the solid discharge variation related to the cross-sectional changes.

$$\frac{\partial A_s}{\partial t} + \xi B\left(\frac{\partial q_s}{\partial A}\frac{dA}{dx} + \frac{\partial q_s}{\partial Q}\frac{dQ}{dx}\right) = -\xi q_s\frac{dB}{dx} \tag{14}$$

2.2. Coupled system of equations

Combining equations (1), (7) and (14), the coupled hydro-morphodynamical system is written in vector form:

$$\frac{\partial \vec{U}}{\partial t} + \boldsymbol{J}(x, \vec{U})\frac{d\vec{U}}{dx} = \vec{S}(x, \vec{U}) \tag{15}$$

$$\vec{U} = (A, Q, A_s)^T$$

$$\boldsymbol{J} = \frac{\partial \vec{F}(x,\vec{U})}{\partial \vec{U}} = \begin{bmatrix} 0 & 1 & 0 \\ c^2 - u^2 & 2u & 0 \\ \xi B \frac{\partial q_s}{\partial A} & \xi B \frac{\partial q_s}{\partial Q} & 0 \end{bmatrix}$$

$$\vec{S}(x,\vec{U}) = \left(0, gA\left[S_0 - S_f - \left(\frac{dh}{dx} - \frac{1}{B}\frac{dA}{dx}\right)\right], -\xi q_s \frac{dB}{dx}\right)^T$$

The conservative fluxes are on the left side of equations, represented by means of the Jacobian matrix $\boldsymbol{J}(x,\vec{U})$. Fluxes purely caused by cross-sectional variations are included as source terms on the right side of equations. $\vec{U}(x,t)$ is the vector of conserved variables, $\boldsymbol{J}(x,\vec{U})$ is the Jacobian matrix, $\vec{S}(x,\vec{U})$ is the source terms vector, $u = Q/A$ is mean flow velocity and $c = \sqrt{g\ A/B}$ is the celerity of the infinitesimal surface wave.

Notice that the Jacobian matrix of the system $\boldsymbol{J}(x,\vec{U})$ is singular, since it does not depend on the third component of the conserved variables vector A_s. This should create difficulties to implement a numerical scheme for this formulation. To overcome this problem, the total bed level can be decomposed into two contributions: a fixed reference level which does not vary with time Z_R and, above that, a layer of erodible sediments with a thickness ϵ_b at the lowest point of the wetted perimeter b, which coincides with the minimum sediment layer depth. Therefore, the bed slope source term can be rewritten as follows:

$$gAS_0 = gA\left[-\frac{d}{dx}(Z_R + \epsilon_b)\right] = -gA\left(\frac{dZ_R}{dx} + \frac{d\epsilon_b}{dx}\right) \tag{16}$$

where $Z_R = Z_R(x)$ and $\epsilon_b = \epsilon_b(x, A_s)$. Therefore, the total derivative of the erodible layer minimum thickness is again expressed as:

$$\frac{d\epsilon_b}{dx} = \left.\frac{\partial \epsilon_b}{\partial x}\right|_{A_s=const} + \left.\frac{\partial \epsilon_b}{\partial A_s}\frac{\partial A_s}{\partial x}\right|_{x=const} = \frac{\partial \epsilon_b}{\partial x} + \frac{\partial \epsilon_b}{\partial A_s}\frac{dA_s}{dx} \tag{17}$$

Replacing (17) in (16) the bed slope source term can be rewritten as:

$$gAS_0 = -c_b^2 \frac{dA_s}{dx} + gAS_0' \tag{18}$$

being:

$$c_b = \sqrt{gA\frac{\partial \epsilon_b}{\partial A_s}} \qquad\qquad S_0' = -\left(\frac{dZ_R}{dx} + \frac{\partial \epsilon_b}{\partial x}\right)$$

The first term on the right hand side of (18) can be considered a new non-conservative momentum flux depending on the solid area changes and it is added to the left side of the momentum equation. The second term on the right hand side of (18) remains as a modified bed slope source term. The coefficient c_b in the non-conservative flux component has velocity dimensions $[L/T]$ and hence it can be considered as a celerity related to the evolution of the lowest point of the bed at each cross-section. This celerity depends on the erosion-deposition mechanism over the channel cross-section, which will be further analyzed in the next sections.

On the other hand, a new partial derivative appears in the modified bed slope source term gAS_0' (18). Following the same procedure used in (7) to properly evaluate the partial derivative of the maximum water depth h [36] and taking into account that $\partial\epsilon_b/\partial A_s = c_b^2/(gA)$, the modified bed slope source term can be rewritten in terms of total derivatives.

$$gAS_0' = -gA\left(\frac{dZ_R}{dx} + \frac{\partial \epsilon_b}{\partial x}\right) = -gA\left[\frac{dZ_R}{dx} + \left(\frac{d\epsilon_b}{dx} - \frac{c_b^2}{gA}\frac{dA_s}{dx}\right)\right] \tag{19}$$

The coupled system (17) can be now expressed in the following non-conservative form:

$$\frac{\partial \vec{U}}{\partial t} + \boldsymbol{J}(x,\vec{U})\frac{d\vec{U}}{dx} + \boldsymbol{H}(x,\vec{U})\frac{d\vec{U}}{dx} = \vec{S}'(x,\vec{U}) \tag{20}$$

$$\vec{U} = (A, Q, A_s)^T$$

$$\boldsymbol{J}(x,\vec{U}) = \begin{bmatrix} 0 & 1 & 0 \\ c^2 - u^2 & 2u & 0 \\ \xi B\frac{\partial q_s}{\partial A} & \xi B\frac{\partial q_s}{\partial Q} & 0 \end{bmatrix} \qquad \boldsymbol{H}(x,\vec{U}) = \begin{bmatrix} 0 & 0 & 0 \\ 0 & 0 & c_b^2 \\ 0 & 0 & 0 \end{bmatrix}$$

$$\vec{S}'(x,\vec{U}) = \begin{bmatrix} 0 \\ -gA\left[\frac{dZ_R}{dx} + \left(\frac{d\epsilon_b}{dx} - \frac{c_b^2}{gA}\frac{dA_s}{dx}\right) + S_f + \left(\frac{dh}{dx} - \frac{1}{B}\frac{dA}{dx}\right)\right] \\ -\xi q_s \frac{dB}{dx} \end{bmatrix}$$

$\boldsymbol{H}(x,\vec{U})$ is the non-conservative flux matrix and $\vec{S}'(x,\vec{U})$ the modified source terms vector. Furthermore, (20) allows us to express the three equations governing the hydro-morphodynamic phenomenon as a reduced system:

$$\frac{\partial \vec{U}}{\partial t} + \boldsymbol{M}(x,\vec{U})\frac{d\vec{U}}{dx} = \vec{S}'(x,\vec{U})$$
$$\boldsymbol{M}(x,\vec{U}) = \boldsymbol{J}(x,\vec{U}) + \boldsymbol{H}(x,\vec{U}) \tag{21}$$

The friction source term is evaluated using the Manning law:

$$S_f = \frac{n^2|u|u}{{R_h}^{4/3}} \tag{22}$$

being n the Manning roughness coefficient and $R_h = A/P$ the hydraulic radius of the cross-section with P the wetted perimeter.

Finally, there only remains the evaluation of the unit solid discharge derivatives ($\partial q_s/\partial A$ and $\partial q_s/\partial Q$) and the bed variation celerity c_b. Therefore, it is necessary to define both the expression for the solid transport rate per unit width (Section 2.3) and the physical mechanism for the cross-section shape actualization (Section 2.4), in order to obtain complete expressions for the governing equations.

2.3. Bed load transport rate

Most of the capacity numerical models that can be found in literature use the Grass law [41] to model the bed load transport rate per unit width $q_s(A,Q)$. For the Grass model, q_s only depends on the hydrodynamical conserved variables A and Q obeying the following expression:

$$q_s(A,Q) = A_g|u|^2u = A_g u^3 \tag{23}$$

where A_g $[s^2/m]$ is a coefficient which takes into account the kinematic viscosity and the grain diameter and is experimentally obtained for each case. Grass model allows us to obtain an explicit expression for the approximate Roe's matrix associated to each local Riemann problem. Following the procedure developed by [32] and extended by [17], the Grass model can be easily adapted to different empirical closure formulae, as Meyer-Peter-Müller model [42], Smart model [43] or Nielsen model [44].

From (23), it is possible to evaluate the third row components of the matrix $\boldsymbol{J}(x,\vec{U})$ in system (20) as follows:

$$J_{31} = \xi B\frac{\partial q_s}{\partial A} = \xi B A_g\frac{\partial u^3}{\partial A} = -\xi B A_g\frac{3u^2}{A}u = -ud$$
$$J_{32} = \xi B\frac{\partial q_s}{\partial Q} = \xi B A_g\frac{\partial u^3}{\partial Q} = \xi B A_g\frac{3u^2}{A} = d \tag{24}$$

2.4. Erosion-deposition mechanism at the cross-section

There is some freedom in the choice of the erosion-deposition mechanism at every cross-section. Three different methods to compute the cross-sectional distribution of the updated solid mass are reported in this section. None of them include information about the streamwise channel curvature, which may be a limitation in meandering rivers. Nevertheless, the proposed methods are enough to approximate the cross-sectional bed evolution in many real-scale morphodynamical flows [11].

As a first and simple approximation, the material of A_s can be assumed to change following horizontal layers [option A]:

$$\text{[Option A]} \quad \frac{\partial \epsilon_b}{\partial A_s} = 1/B_b \qquad c_b^2 = g\frac{A}{B_b} \tag{25}$$

or uniformly at the whole wetted perimeter [option B]:

$$\text{[Option B]} \quad \frac{\partial \epsilon_b}{\partial A_s} = 1/P \qquad c_b^2 = g\frac{A}{P} = gR_h \tag{26}$$

where $B_b(x, A_s)$ is the channel width at the bed level.

However, a more complex mechanism is the evaluation of the bed variation at each point of the cross-section as a function of the boundary shear stress distribution. Following a modified version of the approach reported by [11], the temporal variation of the sediment layer thickness at a partition j of width δy in the channel cross-section ($\Delta\epsilon_j$) can be evaluated as:

$$\Delta\epsilon_j = K_j \frac{\Delta A_s}{\delta y} \tag{27}$$

being ΔA_s the temporal variation of solid area at the whole cross-section and K_j a weighting coefficient calculated as a function of the boundary shear stress at the partition j (Fig. 2). Coefficients K_j for each point of the cross-section are calculated as follows:

1. **Erosion** ($\Delta A_s < 0$)

$$K_j = \frac{(\gamma\tau_j - \tau_{min})^{3/2}}{\sum_j (\gamma\tau_j - \tau_{min})^{3/2}} \qquad \text{with:} \quad \gamma = \frac{\rho_w g R_h |S_f|}{\tau_{min}} \tag{28}$$

2. **Deposition** ($\Delta A_s > 0$)

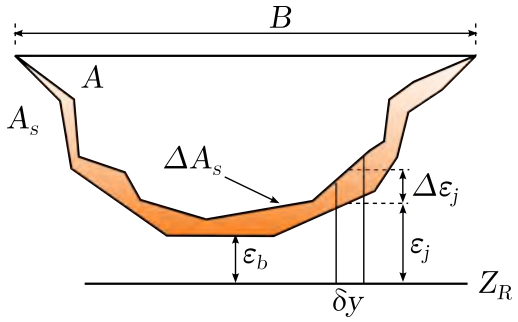

Figure 2: Sketch for the stress cross-section weighted updating mechanism.

$$K_j = \frac{(\tau_{max} - \gamma\tau_j)^{3/2}}{\sum_j (\tau_{max} - \gamma\tau_j)^{3/2}} \qquad \text{with:} \quad \gamma = \frac{\rho_w g R_h |S_f|}{\tau_{max}} \tag{29}$$

where τ_j is the boundary shear stress module at partition j, τ_{min} and τ_{max} are the minimum and maximum (in module) boundary shear stress at the cross-section, respectively. The parameter γ ensures that all the bed points located under the water surface level will be moved upward or downward depending on erosion or deposition taking place and avoiding that K_j becomes nil. The computation of τ_j can be performed in different ways [45–47]. For the type of problems considered in this work, τ_j can be calculated as $\tau_j = \rho_w g h_j |S_f|$ [45].

From expressions (28) and (29) evaluated at the lowest point b of the cross-section $K_j(j \equiv b) = K_b$, the bed variation celerity c_b at the cross-section can be calculated as:

$$\text{[Option C]} \quad \frac{\partial \epsilon_b}{\partial A_s} = \frac{K_b}{\delta y} \qquad c_b^2 = gA\frac{K_b}{\delta y} \tag{30}$$

3. Numerical scheme

The system of equations (21) is solved according to a finite volume method. The domain is divided in computational cells of constant size $\delta x = x_{i+1/2} - x_{i-1/2}$. The coupled system is integrated in each cell and, applying Gauss theorem:

$$\frac{d}{dt}\int_{i-1/2}^{i+1/2} \vec{U} dx + \vec{E}_{i+1/2} - \vec{E}_{i-1/2} = \int_{i-1/2}^{i+1/2} \vec{S}' dx \tag{31}$$

where $\vec{E}_{i+1/2}$ represents the intercell fluxes at the cell face $i+1/2$. We indicate the cell-average value of the solution $\vec{U}(x,t)$ for the cell i at time t^n as $\vec{U}_i^n$, defined as:

$$\vec{U}_i^n = \frac{1}{\delta x}\int_{i-1/2}^{i+1/2} \vec{U}(x,t^n)dx \tag{32}$$

Therefore, assuming a piecewise representation of the conserved variables and fluxes, the first order Godunov's method provides a way to update the averaged values of the solution $\vec{U}_i^n$ to the next time step t^{n+1}. The local Riemann problem associated to each cell face is solved independently and the resulting values for the conserved variables should be cell-averaged again to obtain the updated solution $\vec{U}_i^{n+1}$:

$$\vec{U}_i^{n+1} = \vec{U}_i^n - \frac{\Delta t}{\delta x}\left[\delta\vec{E}|_{i+1/2} - \delta\vec{E}|_{i-1/2}\right] + \Delta t\int_{i-1/2}^{i+1/2}\vec{S'}(x,t^n)dx \tag{33}$$

being $\delta\vec{E}|_{i+1/2} = \vec{E}_{i+1}^n - \vec{E}_i^n$ the difference of the fluxes at the neighbouring cells, including both conservative and non-conservative fluxes. Since the source terms are not necessarily constant, we assume the following linearization:

$$\vec{S'}|_{i+1/2} = \int_i^{i+1}\vec{S'}(x,t^n)dx \tag{34}$$

The numerical scheme could be rewritten as:

$$\vec{U}_i^{n+1} = \vec{U}_i^n - \frac{\Delta t}{\Delta x}\left[(\delta\vec{E} - \vec{S'}\Delta x)|_{i+1/2} - (\delta\vec{E} - \vec{S'}\Delta x)|_{i-1/2}\right] \tag{35}$$

The definition of the numerical scheme in the Godunov's method must be completed by the definition of an approximate solver for the local Riemann problem governed by the fluxes ($\vec{E}_i^n$ and $\vec{E}_{i+1}^n$) and the source terms.

3.1. Roe's approximate solver for the classical Grass model ($A_g = const$)

The solution at the next time $\vec{U}(x,t^{n+1})$ is approximated by cell-averaging the solution of an equivalent linearized Riemann problem associated to each cell face. The integral of the approximate solution $\hat{U}(x,t)$ over a suitable control volume must be equal to the integral of the exact solution over the

same control volume (Consistency Condition). For each edge $i+1/2$, separating cells i and $i+1$, a linearised local RP can be defined, described by the following hyperbolic system of equations:

$$\begin{aligned}
&\frac{\partial \widehat{U}}{\partial t} + \widetilde{\boldsymbol{M}}(\vec{U}_i, \vec{U}_{i+1}) \frac{d\widehat{U}}{dx} = \widetilde{\vec{S}}'(\vec{U}_i, \vec{U}_{i+1}) \\
&\widetilde{\boldsymbol{M}}(\vec{U}_i, \vec{U}_{i+1}) = \widetilde{\boldsymbol{J}}(\vec{U}_i, \vec{U}_{i+1}) + \widetilde{\boldsymbol{H}}(\vec{U}_i, \vec{U}_{i+1}) \\
&\widehat{U}(x,0) = \begin{cases} \vec{U}_i & \text{if } x < 0 \\ \vec{U}_{i+1} & \text{if } x > 0 \end{cases}
\end{aligned} \tag{36}$$

Therefore, two proper linearized matrices $\widetilde{\boldsymbol{J}}(\vec{U}_i, \vec{U}_{i+1})$ and $\widetilde{\boldsymbol{H}}(\vec{U}_i, \vec{U}_{i+1})$ are required, with the following Roe's averaged components:

$$\widetilde{\boldsymbol{J}}(\vec{U}_i, \vec{U}_{i+1}) = \begin{bmatrix} 0 & 1 & 0 \\ \widetilde{c}^2 - \widetilde{u}^2 & 2\widetilde{u} & 0 \\ -\widetilde{u}\widetilde{d} & \widetilde{d} & 0 \end{bmatrix} \qquad \widetilde{\boldsymbol{H}}(\vec{U}_i, \vec{U}_{i+1}) = \begin{bmatrix} 0 & 0 & 0 \\ 0 & 0 & \widetilde{c}_b^{\,2} \\ 0 & 0 & 0 \end{bmatrix} \tag{37}$$

The approximated matrices $\widetilde{\boldsymbol{J}}$ and $\widetilde{\boldsymbol{H}}$ should agree with the main properties for each local Riemann problem:

$$\begin{cases} \delta\vec{F}|_{i+1/2} = \widetilde{\boldsymbol{J}}(\vec{U}_i, \vec{U}_{i+1})\ \delta\vec{U}|_{i+1/2} \\ \widetilde{\boldsymbol{J}}(\vec{U}_i, \vec{U}_{i+1}) = \boldsymbol{J}(\vec{U}_i) \end{cases} \qquad \begin{cases} \vec{T}_b|_{i+1/2} = \widetilde{\boldsymbol{H}}(\vec{U}_i, \vec{U}_{i+1})\ \delta\vec{U}|_{i+1/2} \\ \widetilde{\boldsymbol{H}}(\vec{U}_i, \vec{U}_{i+1}) = \boldsymbol{H}(\vec{U}_i) \end{cases} \tag{38}$$

being $\delta\vec{F}|_{i+1/2}$ and $\vec{T}_b|_{i+1/2}$ the conservative fluxes jump and the non-conservative flux vectors, respectively, at the interface $i+1/2$. Application of conditions (38) leads to the Roe's averaged quantities for the velocity $\widetilde{u}$, the infinitesimal waves celerity $\widetilde{c}$ and the solid discharge derivative $\widetilde{d}$.

$$\begin{aligned}
&\widetilde{c} = \sqrt{g\frac{A_i + A_{i+1}}{B_i + B_{i+1}}} \qquad \widetilde{u} = \frac{u_i\sqrt{A_i} + u_{i+1}\sqrt{A_{i+1}}}{\sqrt{A_i} + \sqrt{A_{i+1}}} \\
&\widetilde{d} = \xi \bar{B} A_g (u_i^2 + u_{i+1}^2 + u_i u_{i+1}) \frac{\sqrt{A_i} + \sqrt{A_{i+1}}}{\sqrt{A_i}A_{i+1} + A_i\sqrt{A_{i+1}}}
\end{aligned} \tag{39}$$

being $\bar{B} = (B_i + B_{i+1})/2$.

On the other hand, it is possible to approximate the non-conservative flux vector at the intercell edge $i+1/2$ in the following way:

$$\vec{T}_b|_{i+1/2} = \left(0,\ g\bar{A}\overline{\frac{\partial \epsilon_b}{\partial A_s}}\delta A_s|_{i+1/2},\ 0\right)^T \tag{40}$$

Considering again the set of conditions (38), the definition of an explicit expression for the averaged value of the bed variation celerity $\widetilde{c}_b$ is straightforward:

$$\widetilde{c}_b = \sqrt{g\bar{A}\overline{\frac{\partial \epsilon_b}{\partial A_s}}} \tag{41}$$

with $\bar{A} = (A_i + A_{i+1})/2$ and $\overline{\frac{\partial \epsilon_b}{\partial A_s}} = \left[\left(\frac{\partial \epsilon_b}{\partial A_s}\right)_i + \left(\frac{\partial \epsilon_b}{\partial A_s}\right)_{i+1}\right]/2$.

Therefore, by simply rewriting $\widetilde{\boldsymbol{M}}(\vec{U}_i, \vec{U}_{i+1}) = \widetilde{\boldsymbol{J}}(\vec{U}_i, \vec{U}_{i+1}) + \widetilde{\boldsymbol{H}}(\vec{U}_i, \vec{U}_{i+1})$ the complete linearized matrix for the coupled system (36), which should be solved at each intercell edge, can be obtained.

$$\widetilde{\boldsymbol{M}}(\vec{U}_i, \vec{U}_{i+1}) = \begin{bmatrix} 0 & 1 & 0 \\ \widetilde{c}^2 - \widetilde{u}^2 & 2\widetilde{u} & \widetilde{c}_b{}^2 \\ -\widetilde{u}\widetilde{d} & \widetilde{d} & 0 \end{bmatrix} \tag{42}$$

Although similar Roe's averaged quantities were reported by [30] for a 1D unit-width coupled scheme, this is the first time –to the authors knowledge– that these analytical expressions have been obtained for cross-section averaged models.

3.1.1. Eigenstructure

The analysis of the eigenstructure of the matrix $\widetilde{\boldsymbol{M}}$ is of interest. Previous efforts in this sense and dealing with bed load and suspended load were reported in [48, 49]. [2] and [3] proposed expressions to approximate the hyperbolic system eigenvalues for the 1D erosive bed load problem, but they did not consider irregular topography neither the influence of the cross-section update mechanism on the characteristic wave celerities.

The eigenvalues of the hyperbolic system (36), describing each local Riemann problem, are the roots of the characteristic polynomial of matrix $\widetilde{\boldsymbol{M}}(\vec{U}_i, \vec{U}_{i+1})$, defined as:

$$P_{\widetilde{M}}(\widetilde{\lambda}) = |\widetilde{\boldsymbol{M}} - \widetilde{\lambda}\boldsymbol{I}| = -\widetilde{\lambda}\left[(\widetilde{u} - \widetilde{\lambda})^2 - \widetilde{c}^2\right] + \widetilde{c}_b{}^2\widetilde{d}\,(\widetilde{\lambda} - \widetilde{u}) = 0 \tag{43}$$

Therefore, the roots of $P_{\widetilde{M}}(\widetilde{\lambda})$ could be understood as the intersection of a cubic polynomial $f_1(\widetilde{\lambda}) = \widetilde{\lambda}\left[(\widetilde{u}-\widetilde{\lambda})^2 - \widetilde{c}^2\right]$ (related to the hydrodynamic component of the coupled system) with the straight line $f_2(\widetilde{\lambda}) = \widetilde{c_b}^2\widetilde{d}\,(\widetilde{\lambda}-\widetilde{u})$, related to the morphodynamic component. As [50] and [26] pointed out in the particular case of unit width rectangular channels, this kind of hyperbolic systems has always two eigenvalues of the same sign as the flow velocity and another one with opposite sign (Fig. 3), regardless of the flow regime.

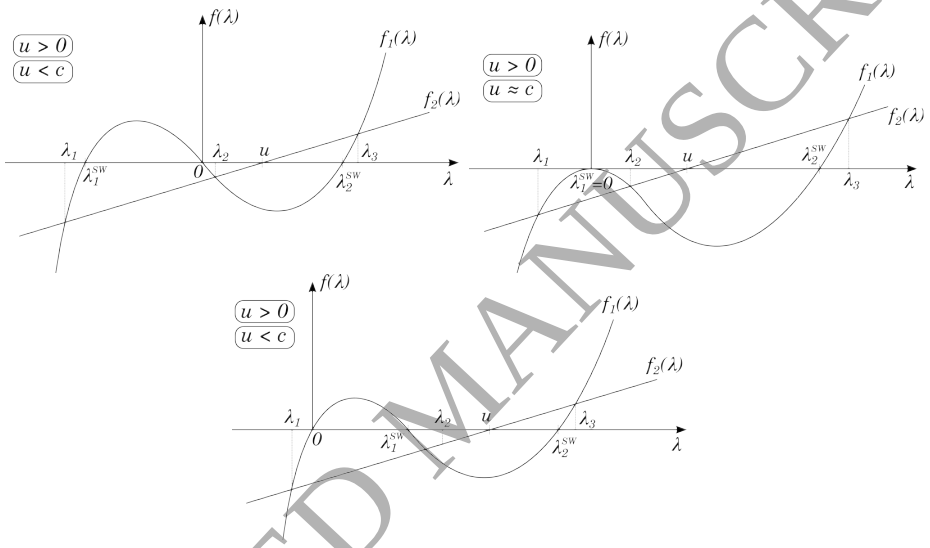

Figure 3: Eigenvalues scheme for the linearized coupled system: (top left) subcritical regime, (top right) critical regime and (bottom) supercritical regime. Flow averaged velocity is considered positive $\widetilde{u} > 0$.

On the other hand, the roots of $P_{\widetilde{M}}(\widetilde{\lambda})$ could also be calculated by the *Cardano-Vieta* formula, considering the complete form of the characteristic polynomial $P_{\widetilde{M}}(\widetilde{\lambda})$:

$$\begin{gathered} P_{\widetilde{M}}(\widetilde{\lambda}) = -\widetilde{\lambda}^3 + 2\widetilde{u}\widetilde{\lambda}^2 + \left(\widetilde{c}^2 - \widetilde{u}^2 + \widetilde{c_b}^2\widetilde{d}\right)\widetilde{\lambda} - \widetilde{c_b}^2\widetilde{u}\widetilde{d} = 0 \\ \widetilde{\lambda}^3 + a_1\widetilde{\lambda}^2 + a_2\widetilde{\lambda} + a_3 = 0 \\ \text{with:} \qquad a_1 = -2\widetilde{u} \qquad a_2 = \widetilde{u}^2 - \widetilde{c}^2 - \widetilde{c_b}^2\widetilde{d} \qquad a_3 = \widetilde{c_b}^2\widetilde{u}\widetilde{d} \end{gathered} \tag{44}$$

$$\widetilde{\lambda}_1 = 2\sqrt{-L}\ cos(\theta/3) - a_1/3$$
$$\widetilde{\lambda}_2 = 2\sqrt{-L}\ cos(\theta/3 + 2\pi/3) - a_1/3$$
$$\widetilde{\lambda}_3 = 2\sqrt{-L}\ cos(\theta/3 + 4\pi/3) - a_1/3$$
$$\text{where :} \qquad L = \frac{3a_2 - a_1^2}{9} \qquad \theta = acos\left(\frac{R}{\sqrt{-L^3}}\right) \qquad R = \frac{9a_1a_2 - 27a_3 - 2a_1^3}{54}$$

The system is strictly hyperbolic if $L^3 + R^2 > 0$. For cases with q_s evaluated by the classical Grass model ($A_g = const$), that is always true. For cases with q_s evaluated by other empirical models, the only condition necessary to ensure the hyperbolicity is $|\widetilde{u}| < 6\widetilde{c}$ [26].

Moreover, the influence of the cross-section updating mechanism (see Section 2.4) on the hydro-morphological model is incorporated by means of the bed variation celerity c_b into the coupled conservative system solution. The selection of a specific mechanism modifies the averaged waves celerity and the whole eigenstructure of the local RP. Fig. 4-left shows a comparison of the coupled eigenvalues $\widetilde{\lambda}_1$, $\widetilde{\lambda}_2$ and $\widetilde{\lambda}_3$ with the common values for the fixed-bed shallow water problem ($\widetilde{u} - \widetilde{c}$ and $\widetilde{u} + \widetilde{c}$). The influence of the morphodynamical updating criteria in the coupled eigenstructure increases for the stress weighted erosion mechanism and is less marked for the stress weighted deposition (both option C). Moreover, this influence also increases as the Froude number increases, separating the coupled eigenvalues $\widetilde{\lambda}_1$ and $\widetilde{\lambda}_3$ from those characteristic of the shallow water system, regardless of the cross-section change criterion adopted (see Fig. 4-left). This fact affects the stability region of the problem and hence the model efficiency. Deposition in horizontal layers (option A) and uniform erosion-deposition (option B) show an intermediate behaviour between those reported for the option C.

Furthermore, the bed variation celerity does not depend on the flow features, even for the mechanism C. This proves that c_b is a geometrical parameter related to the cross-sectional shape, regardless of the erosion-deposition mechanism selected (Fig. 4-right).

The right eigenvectors basis $\widetilde{\vec{e}}_m$ for the system can be calculated as:

$$\widetilde{\boldsymbol{M}}\widetilde{\vec{e}}_m = \widetilde{\lambda}_m\widetilde{\vec{e}}_m \tag{45}$$

By setting $\widetilde{e}_m^1 = 1$, one can obtain the values for the second component $\widetilde{e}_m^2$ and the third component $\widetilde{e}_m^3$ of the right eigenvectors:

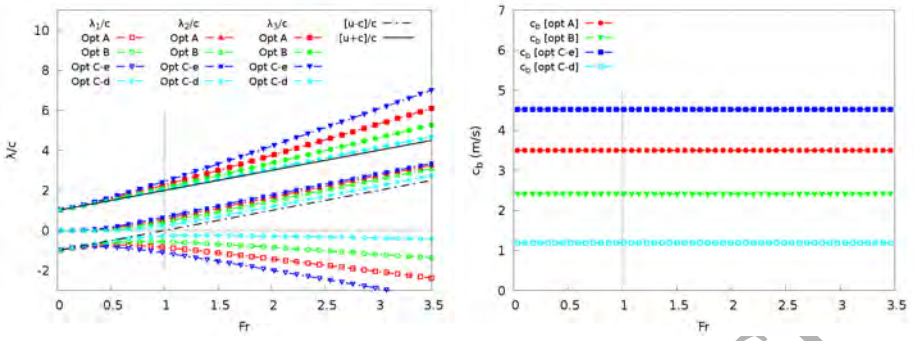

Figure 4: (Left) Eigenvalues of the coupled system $\widetilde{\lambda}_1$, $\widetilde{\lambda}_2$ and $\widetilde{\lambda}_3$ and (right) bed variation celerity c_b as a function of the Froude number for a trapezoidal cross-section, depending on the cross-section updating mechanism.

$$\widetilde{\vec{e}}_m = \left(1, \widetilde{\lambda}_m, \frac{(\widetilde{\lambda}_m - \widetilde{u})^2 - \widetilde{c}^2}{\widetilde{c_b}^2}\right)^T \tag{46}$$

Finally, conserved variable differences $\delta\vec{U}|_{i+1/2}$ and source term integrals $\widetilde{\vec{S}'}\Delta x|_{i+1/2}$ at the intercell edge $i+1/2$ are projected on the eigenvector basis $\widetilde{\vec{e}}_m$ in order to obtain the wave and source strengths, $\widetilde{\alpha}_m$ and $\widetilde{\beta}_m$ respectively.

$$\begin{aligned} \delta\vec{U}|_{i+1/2} &= \sum_m \widetilde{\alpha}_m \widetilde{\vec{e}}_m \\ \widetilde{\vec{S}'}\Delta x|_{i+1/2} &= \sum_m \widetilde{\beta}_m \widetilde{\vec{e}}_m \end{aligned} \tag{47}$$

A complete description of the explicit expressions obtained for the wave and source strengths can be found in Appendix A, together with other aspects related to the averaged source terms computation.

Therefore, it is possible to express the flux differences and the source terms integral at the intercell edge $i+1/2$ as their projection onto the right eigenvector basis of the approximate Jacobian matrix of the hyperbolic system (36):

$$(\delta\vec{E} - \vec{S}'\Delta x)|_{i+1/2} = \sum_m \left(\widetilde{\lambda}_m \widetilde{\alpha}_m - \widetilde{\beta}_m\right) \widetilde{\vec{e}}_m \Big|_{i+1/2} \tag{48}$$

Finally, the augmented Roe's upwind scheme considering $A_g = cte$ through the intercell edge is written as:

$$\vec{U}_i^{n+1} = \vec{U}_i^n - \frac{\Delta t}{\Delta x}\left[\sum_m \left(\widetilde{\lambda}_m^+ \widetilde{\alpha}_m - \widetilde{\beta}_m\right)\widetilde{\vec{e}}_m\Big|_{i-1/2} + \sum_m \left(\widetilde{\lambda}_m^- \widetilde{\alpha}_m - \widetilde{\beta}_m\right)\widetilde{\vec{e}}_m\Big|_{i+1/2}\right]$$
$$\text{with:} \quad \widetilde{\lambda}_m^{\pm} = \frac{\widetilde{\lambda}_m \pm |\widetilde{\lambda}_m|}{2} \tag{49}$$

3.2. Roe's approximate solver for empirical models ($A_g \neq const$)

In realistic applications, the solid transport rate is evaluated as a function of the bottom shear stress τ. To estimate a value for the solid transport rate per unit width, any of the experimental models published in literature could be considered. [32] and [17] reported a method to adjust the Grass model to these empirical formulae. The method simply modifies the Grass coefficient value as a function, leading to different Grass coefficients A_g in the cells i and $i+1$. In these cases, and following [32], it is possible to evaluate the solid discharge at each side of the cell face considering an averaged Grass coefficient $\bar{A}_g|_{i+1/2}$:

$$\begin{aligned} \bar{A}_g|_{i+1/2} &= \frac{A_{gi} + A_{gi+1}}{2} \\ \bar{Q}_{si} = Q_s(\bar{A}_g|_{i+1/2}, \vec{U}_i) \qquad & \bar{Q}_{si+1} = Q_s(\bar{A}_g|_{i+1/2}, \vec{U}_{i+1}) \\ Q_{si} = Q_s(A_{gi}, \vec{U}_i) \qquad & Q_{si+1} = Q_s(A_{gi+1}, \vec{U}_{i+1}) \end{aligned} \tag{50}$$

Therefore, the total flux differences at the intercell $i+1/2$ can be written as:

$$\delta Q_s|_{i+1/2} = \delta \bar{Q}_s|_{i+1/2} + \delta(Q_s - \bar{Q}_s)|_{i+1/2} \tag{51}$$

with:

$$\begin{aligned} \delta Q_s|_{i+1/2} &= Q_{si+1} - Q_{si} \\ \delta \bar{Q}_s|_{i+1/2} &= \bar{Q}_{si+1} - \bar{Q}_{si} \\ \delta(Q_s - \bar{Q}_s)|_{i+1/2} &= \underbrace{(Q_{si+1} - \bar{Q}_{si+1})}_{\text{Cell i+1}} - \underbrace{(Q_{si} - \bar{Q}_{si})}_{\text{Cell i}} \end{aligned} \tag{52}$$

Therefore, $\delta\bar{Q}_s|_{i+1/2}$ is evaluated by the Roe's method considering a non-conservative Jacobian matrix, leading to the scheme (49). However, to ensure bed load conservation, the solid flux difference $\delta(Q_s - \bar{Q}_s)|_{i+1/2}$ should be included by means of a new cellwise contribution which does not require any splitting [32].

$$\vec{U}_i^{n+1} = \vec{U}_i^n - \frac{\Delta t}{\Delta x}\left[\sum_m \left(\widetilde{\lambda}_m^+ \widetilde{\alpha}_m - \widetilde{\beta}_m\right)\widetilde{\vec{e}}_m\Big|_{i-1/2} + \sum_m \left(\widetilde{\lambda}_m^- \widetilde{\alpha}_m - \widetilde{\beta}_m\right)\widetilde{\vec{e}}_m\Big|_{i+1/2}\right] - \frac{\Delta t}{\Delta x}\left[\delta\vec{F}_i^*\Big|_{i-1/2} + \delta\vec{F}_i^*\Big|_{i+1/2}\right] \tag{53}$$

being:

$$\begin{aligned}\delta\vec{F}_i^*\Big|_{i-1/2} &= \left[0,\ 0,\ \xi B_i|u_i|^2 u_i(A_{gi} - \bar{A}_g|_{i-1/2})\right]^T \\ \delta\vec{F}_i^*\Big|_{i+1/2} &= \left[0,\ 0,\ \xi B_i|u_i|^2 u_i(\bar{A}_g|_{i+1/2} - A_{gi})\right]^T\end{aligned} \tag{54}$$

Following [32], from now on, the updating numerical scheme (53) will be referred as Conservative Coupled Model (CCM) to clearly distinguish it from the numerical scheme (49), which will be called as NCCM (Non-Conservative Coupled Model).

3.3. Numerical fixes

3.3.1. Wetted area positivity

The cell averaging process could lead to unphysical negative wetted area values due to the local Riemann problem linearization process at the cell interfaces [51]. This problem can be avoided by enforcing positivity on the wetted area values of the RP intermediate states. Following the formulation in [37], the wetted area intermediate values considering right flow direction ($\widetilde{u} > 0$) can be expressed as:

$$
\begin{aligned}
A_i^* &= A_i^n + \left(\widetilde{\alpha}_1 - \frac{\widetilde{\beta}_1}{\widetilde{\lambda}_1}\right) \\
A_{i+1}^{***} &= A_{i+1}^n - \left(\widetilde{\alpha}_3 - \frac{\widetilde{\beta}_3}{\widetilde{\lambda}_3}\right) \\
A_{i+1}^{**} &= A_{i+1}^{***} - \left(\widetilde{\alpha}_2 - \frac{\widetilde{\beta}_2}{\widetilde{\lambda}_2}\right)
\end{aligned}
\tag{55}
$$

being $\widetilde{\lambda}_1 < 0$ and $\widetilde{\lambda}_2, \widetilde{\lambda}_3 > 0$.

Positive values of the wetted area intermediate states (A^*, A^{**}, A^{***}) are enforced by a proper reconstruction of the source strength β_m values. This limitation is only applied to wet-wet walls since in dry-wet walls the appearance of negatives values of A^*, A^{**}, A^{***} in the approximate solution is helpful to provide a correct tracking of the flood advance.

Unlike fixed bed cases, with movable bed there always exists a wave moving upstream. The advantage is that the numerical method does not require the usual entropy correction. The drawback is that the cell averaging process does not ensure positivity of the solution in supercritical cases. Therefore the intermediate states positivity control is also needed in supercritical regimes.

Enforcing $A^*, A^{**}, A^{***} \geq 0$, minimum values for the corresponding source strengths $\widetilde{\beta}_m$ can be derived:

$$
\begin{aligned}
\widetilde{\beta}_{1min} &= -A_i^n|\widetilde{\lambda}_1| - |\widetilde{\lambda}_1|\widetilde{\alpha}_1 \\
\widetilde{\beta}_{3min} &= -A_{i+1}^n\widetilde{\lambda}_3 + \widetilde{\lambda}_3\widetilde{\alpha}_3 \\
\widetilde{\beta}_{2min} &= -A_{i+1}^{***}\widetilde{\lambda}_2 + \widetilde{\lambda}_2\widetilde{\alpha}_2
\end{aligned}
\tag{56}
$$

In the case $A_i^* < 0$, the new value of $\widetilde{\beta}_1$ is redefined as $\widetilde{\beta}_{1min}$. To ensure conservation, $\widetilde{\beta}_2$ and $\widetilde{\beta}_3$ should be redefined according to:

$$
\begin{aligned}
&\widetilde{\beta}_1 + \widetilde{\beta}_2 + \widetilde{\beta}_3 = 0 \\
&\widetilde{\beta}_1\widetilde{e}_1^3 + \widetilde{\beta}_2\widetilde{e}_2^3 + \widetilde{\beta}_3\widetilde{e}_3^3 = \bar{S}'_3\Delta x
\end{aligned}
\tag{57}
$$

This lead to new values for all source strengths:

$$\begin{aligned}\widetilde{\beta}_1 &= \widetilde{\beta}_{1min}\\ \widetilde{\beta}_3 &= \frac{\bar{S'}_3\Delta x - \widetilde{\beta}_1(\widetilde{e}_1^3 - \widetilde{e}_2^3)}{\widetilde{e}_3^3 - \widetilde{e}_2^3}\\ \widetilde{\beta}_2 &= -(\widetilde{\beta}_1 + \widetilde{\beta}_3)\end{aligned} \tag{58}$$

It is necessary to check that $\widetilde{\beta}_2 \geq \widetilde{\beta}_{2min}$ and $\widetilde{\beta}_3 \geq \widetilde{\beta}_{3min}$ to ensure that A_{i+1}^{**} and A_{i+1}^{***} remain also positive. This procedure could be extended in a similar way to the cases $A_{i+1}^{**} < 0$ and $A_{i+1}^{***} < 0$.

3.3.2. Reduction to non-movable bed flow

During a dynamical erosive event, it is possible that erosion-deposition is not active in some intercell edges. Therefore, for these cases the numerical scheme should reduce to the shallow water flow over non-movable bed solution. Basically this is a consequence of the shear stress on the channel bottom τ in two consecutive cells being lower than the threshold τ_c, hence the solid discharge does not exist through the edge connecting these two cells.

In this case, the Grass coefficient at both cells is set to zero ($A_{gi} = A_{gi+1} = 0$) and the solid discharge derivative $\widetilde{d}|_{i+1/2}$ is nil. Considering $\widetilde{u} > 0$ the Roe's averaged eigenvalues at the intercell edge $i + 1/2$ evolve as follows:

1. Subcritical case:

$$\begin{aligned}&\widetilde{\lambda}_1 = \widetilde{u} - \widetilde{c} < 0 && \widetilde{\lambda}_2 = 0 && \widetilde{\lambda}_3 = \widetilde{u} + \widetilde{c} > 0\\ &\widetilde{\vec{e}}_1 = (1, \widetilde{u} - \widetilde{c}, 0)^T && \widetilde{\vec{e}}_2 = \left(1, 0, \frac{\widetilde{u}^2 - \widetilde{c}^2}{\widetilde{c_b}^2}\right)^T && \widetilde{\vec{e}}_3 = (1, \widetilde{u} + \widetilde{c}, 0)^T\end{aligned} \tag{59}$$

2. Supercritical case:

$$\begin{aligned}&\widetilde{\lambda}_1 = 0 && \widetilde{\lambda}_2 = \widetilde{u} - \widetilde{c} > 0 && \widetilde{\lambda}_3 = \widetilde{u} + \widetilde{c} > 0\\ &\widetilde{\vec{e}}_1 = \left(1, 0, \frac{\widetilde{u}^2 - \widetilde{c}^2}{\widetilde{c_b}^2}\right)^T && \widetilde{\vec{e}}_2 = (1, \widetilde{u} - \widetilde{c}, 0)^T && \widetilde{\vec{e}}_3 = (1, \widetilde{u} + \widetilde{c}, 0)^T\end{aligned} \tag{60}$$

Therefore, one of the original genuinely non-linear characteristic fields of the coupled system evolves to a linearly degenerated field ($\widetilde{\lambda}_2$ for subcritical cases and $\widetilde{\lambda}_1$ for supercritical cases), appearing a contact wave caused by the non-conservative flux included in the Jacobian Roe's matrix [52].

In cases where a rarefaction wave with a critical point exists, the flow changes from subcritical to supercritical regime at cells i and $i+1$, respectively (Fig. 5). In this situation, transonic rarefaction phenomena could not be evaluated by the numerical scheme properly without an entropy-preserving redistribution of the affected waves.

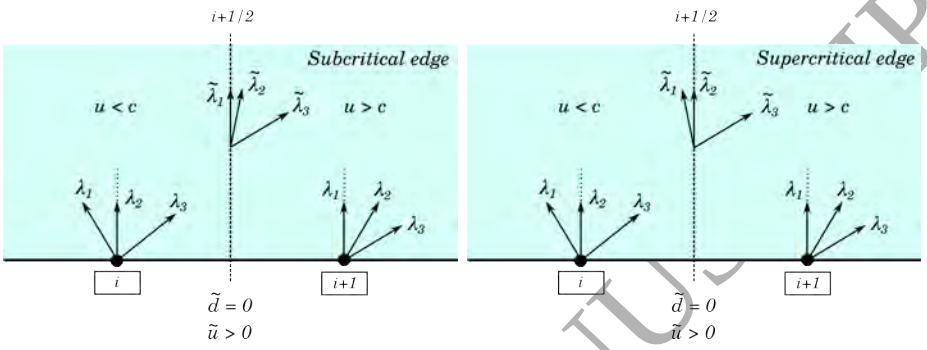

Figure 5: Wave orientation at cells and intercell edge for a trans-sonic rarefaction wave case with non-movable bed: (left) subcritical edge case and (right) supercritical edge case.

In the particular case when rarefaction wave appears at any intercell edge with a bed discontinuity, the implementation of the classical [53] entropy fix has been found not to be directly applicable due to the presence of two overlapping contact waves, one generated by the source terms and one caused by the non-conservative flux associated to a bed discontinuity [52]. Therefore, in these cases a correction on the wave and source strengths must be done, restoring the non-conservative flux to the bed slope source term.

Considering the subcritical case ($\widetilde{\lambda}_2 = 0$), the corrected values of $\widetilde{\alpha}'$ and $\widetilde{\beta}'$ are computed in the following way:

$$\begin{aligned} \widetilde{\alpha}'_1 &= \widetilde{\alpha}_1 + \frac{\widetilde{c_b}^2 \delta A_s}{2\widetilde{c}(\widetilde{u}-\widetilde{c})} & \widetilde{\alpha}'_2 &= 0 & \widetilde{\alpha}'_3 &= \widetilde{\alpha}_3 - \frac{\widetilde{c_b}^2 \delta A_s}{2\widetilde{c}(\widetilde{u}+\widetilde{c})} \\ \widetilde{\beta}'_1 &= \widetilde{\beta}_1 + \frac{\widetilde{c_b}^2 \delta A_s}{2\widetilde{c}} & \widetilde{\beta}'_2 &= 0 & \widetilde{\beta}'_3 &= \widetilde{\beta}_3 - \frac{\widetilde{c_b}^2 \delta A_s}{2\widetilde{c}} \end{aligned} \tag{61}$$

Finally, an efficient entropy-preserving correction could be computed by affecting the waves celerity and source strengths as follows:

$$\lambda_1^L = u_i - c_i < 0 \qquad \lambda_2^L = 0 \qquad \lambda_3^L = u_i + c_i > 0$$
$$\lambda_1^R = 0 \qquad \lambda_2^R = u_{i+1} - c_{i+1} > 0 \qquad \lambda_3^R = u_{i+1} + c_{i+1} > 0$$

$$\lambda_I = \lambda_1^L \frac{\lambda_2^R - \widehat{\lambda}}{\lambda_2^R - \lambda_1^L} \qquad \lambda_J = \lambda_2^R \frac{\widehat{\lambda} - \lambda_1^L}{\lambda_2^R - \lambda_1^L} \tag{62}$$

So that $\widehat{\lambda} = \lambda_I + \lambda_J$, being:

$$\widehat{\lambda} = \begin{cases} \widetilde{\lambda}_1 & \text{if } \widetilde{\lambda}_1 \neq 0 \\ \widetilde{\lambda}_2 & \text{if } \widetilde{\lambda}_2 \neq 0 \end{cases} \tag{63}$$

Concerning the source strength, the new redistributed values can be expressed as follows:

$$\widehat{\beta} = \beta_I + \beta_J \qquad \text{with:} \qquad \beta_I = \widehat{\beta} \qquad \beta_J = 0 \tag{64}$$

being:

$$\widehat{\beta} = \begin{cases} \widetilde{\beta'}_1 & \text{if } \widetilde{\lambda}_1 \neq 0 \\ \widetilde{\beta'}_2 & \text{if } \widetilde{\lambda}_2 \neq 0 \end{cases}$$

The wave with the subscript I affects the left cell ($\lambda_I < 0$), whereas the wave with the subscript J affects to right cell ($\lambda_J > 0$).

3.4. Stability region

For each intercell edge $i+1/2$, the time step should be dynamically limited to ensure that there is no interaction of waves from neighboring Riemann problems. If the positivity of all wetted area values in the intermediate states of the solution is guaranteed (see Section 3.3.1) $A_i^* \geq 0$, $A_i^{**} \geq 0$ and $A_i^{***} \geq 0$, in order to construct an updated cell average solution $\vec{U}_i^{n+1}$, it is only necessary that the edge values $\widehat{U}(x,t)$ remain constant in time over the entire time step. This unique requirement allows us to define an upper limit for the time step depending only on the characteristic waves celerity and the spatial cell size. In consequence, the stability region at the intercell edge k is defined as:

$$\Delta t \leq \Delta t^{\widetilde{\lambda}}|_k \qquad \Delta t^{\widetilde{\lambda}}|_k = \frac{\Delta x}{\max\limits_m(|\widetilde{\lambda}_m|)} \tag{65}$$

Therefore, the global time step for the updated solution calculation is obtained applying a CFL condition:

$$\Delta t = \text{CFL} \min_{k=1}^{N}(\Delta t^{\tilde{\lambda}}|_k) \tag{66}$$

where CFL ≤ 1 and N is the total number of local RP which should be solved at each time calculation.

4. Numerical tests

4.1. Performance of the model in non-movable bed conditions

In non-movable bed conditions, the numerical scheme should reduce to the common shallow water solution for variable cross-section channels [37]. The performance of the model in these conditions was tested by means of two ideal dam-break flows over a rigid bed step. The Grass coefficient A_g was set nil at the whole domain. Initial conditions are summarized in Table 1. The domain was a prismatic rectangular cross-section channel with $B_b = 1\ m$ and 30 m length. The solution was evolved to a final time $t = 1\ s$ with CFL = 1.

Test	h_L (m)	h_R (m)	u_L (m/s)	u_R (m/s)	ϵ_{bL} (m)	ϵ_{bR} (m)	A_g
Test 1	3.5	1.5	0	0	1.5	1.0	0
Test 2	15.5	1.5	0	0	2.0	1.0	0

Table 1: Summary of the dam-break over non-movable bed step test cases.

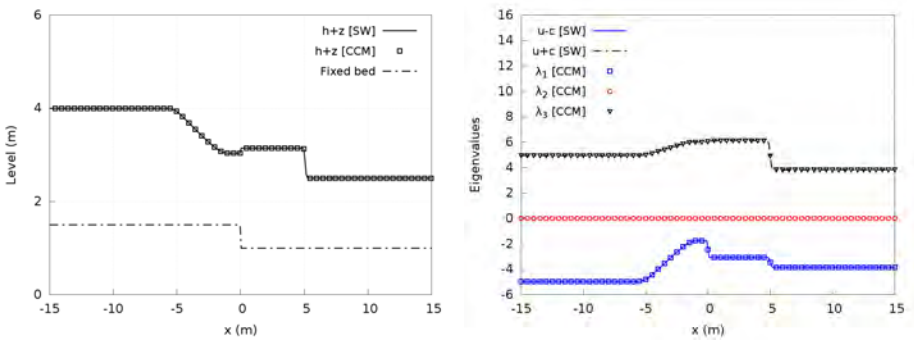

Figure 6: Free-surface level (left) and eigenvalues at t = 1 s (right) for subcritical dam-break with non-movable bed conditions.

In Test 1 (Fig. 6) the unsteady flow remains always subcritical and the erosive coupled model eigenvalues $\widetilde{\lambda}_1$ and $\widetilde{\lambda}_3$ reduce to the common wave celerities for the shallow water scheme, $\widetilde{u} - \widetilde{c}$ and $\widetilde{u} + \widetilde{c}$, whereas the second eigenvalue $\widetilde{\lambda}_2$ remains nil for all the simulated times.

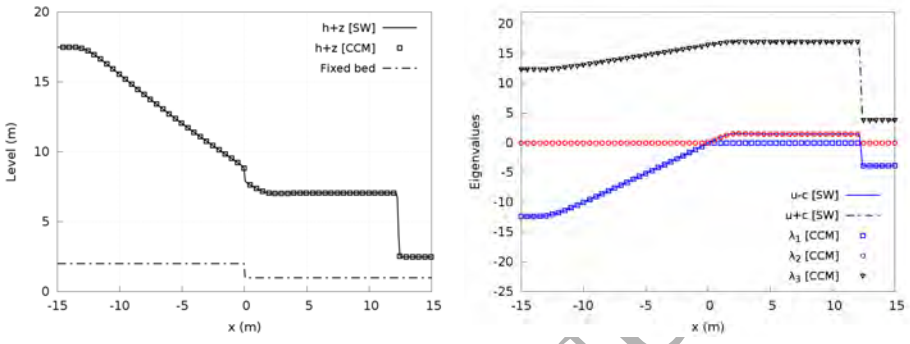

Figure 7: Free-surface level (left) and eigenvalues at t = 1 s (right) for supercritical dam-break with non-movable bed conditions.

However, for Test 2 (Fig. 7), the flow regime changes from subcritical upstream to supercritical downstream the bed step. At the subcritical flow reach, the first eigenvalue $\widetilde{\lambda}_1 = \widetilde{u} - \widetilde{c}$ and the second one is nil. Nevertheless, at the supercritical reach $\widetilde{\lambda}_2 = \widetilde{u} - \widetilde{c}$ and λ_1 becomes nil. Therefore, an entropy fix is needed to keep a physically proper numerical solution at the bed step. The third eigenvalue is $\widetilde{\lambda}_3 = \widetilde{u} + \widetilde{c}$, regardless of the flow regime. Moreover, the free-surface level predicted by the CCM model agrees perfectly with the original shallow water scheme in both subcritical and supercritical cases. Therefore, the CCM model is able to reduce accurately to the original shallow water model for intercell edges in which erosion phenomena do not exist.

4.2. Equilibrium slopes for steady flow regimes

The aim of these test cases is to assess the ability of the proposed method to converge to the exact solution in erosive steady flow regimes, behaving in a well-balanced form. The geometry for test A and B is a rectangular channel with constant width $B_b = 1\ m$ (Fig. 8). The inlet discharge is constant ($Q_{IN} = 1\ m^3/s$) and the bed layer thickness at the inlet is set to $\epsilon_b(x = 0) = 2\ m$. The initial flow conditions correspond to a uniform regime with $Q = 1\ m^3/s$, $S_0 = 0.002$ and $n = 0.02 s m^{-1/3}$. The water depth at

the channel outlet is set to $h(x = 100) = 0.943\ m$, corresponding to the constant water depth above the uniform regime. The equilibrium bed slope for uniform flow in prismatic rectangular channels ($S_0 = S_f$) is considered here as exact solution. The simulation was evolved until it reached the steady state with a constant Grass coefficient $A_g = 0.01$ in all the test cases. All the simulations were made with CFL = 1, $\Delta x = 1\ m$.

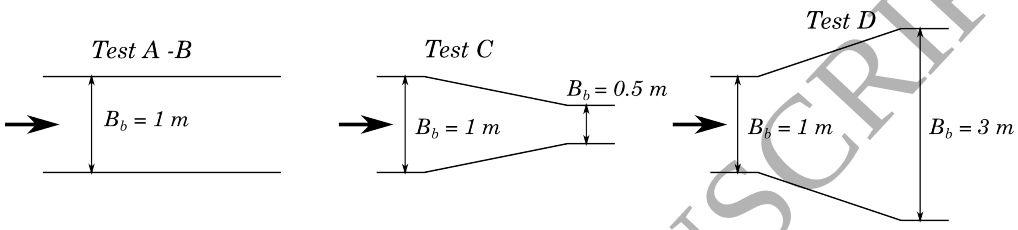

Figure 8: Width variation scheme for (left) tests A and B, (center) test C and (right) test D.

In test A (Fig. 9-left), the initial bed slope was set to $S_0 = 0.007$, higher than the equilibrium slope in uniform regime. The numerical solution progressively adapts the bed level by sediment deposition until the steady state for $S_0 = 0.002$ is reached. In test B (Fig. 9-right) the numerical method also moves the bed level progressively by an erosion mechanism, from an initial flat bottom to the equilibrium exact solution.

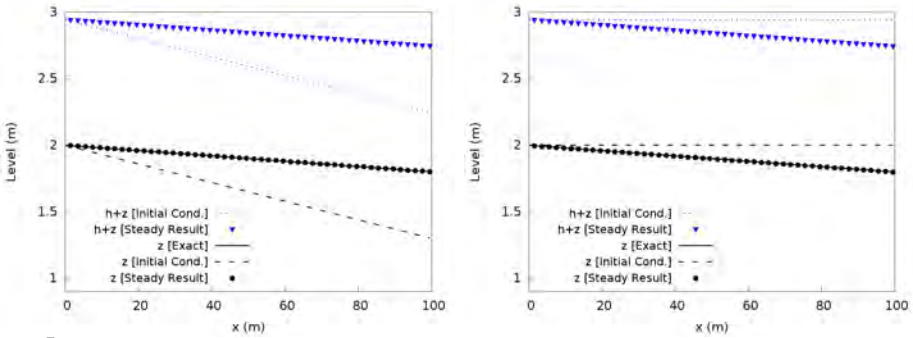

Figure 9: Numerical results and exact solution for steady states in prismatic rectangular cross-section channels: (left) Test A with bed deposition and (right) Test B with bed erosion.

The geometry for variable cross-section cases was a rectangular channel with linearly variable width from $B_b = 1\ m$ at $x = 20\ m$ to $B_b = 0.5\ m$ (Test

C) and $B_b = 3.0\ m$ (Test D) at $x = 80\ m$ (Fig. 8). Discharge and bed level at the inlet were set to 1 m^3/s and 2 m, respectively. The initial bed slope was set to $S_0 = 0.002$ in both cases. The goal of these tests is to evaluate the influence of the width variation on the bed level evolution respect to a stable state for a prismatic rectangular cross-section channel. Initial flow conditions were the same as in tests A and B and the output water depth boundary condition was that corresponding to a uniform flow in a prismatic channel of $B_b = 0.5\ m$ (Test C) and $B_b = 3\ m$ (Test D).

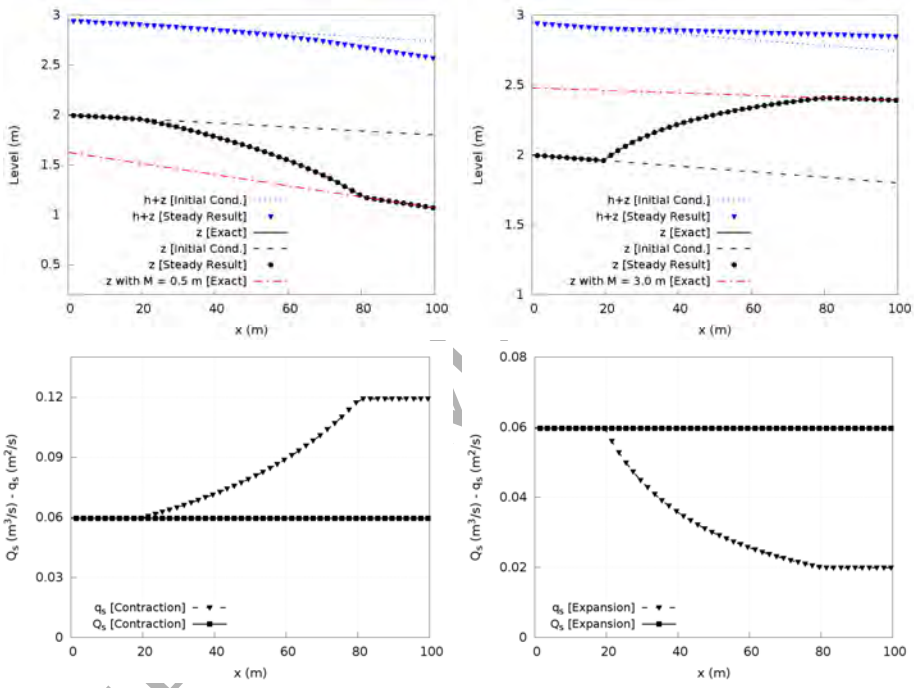

Figure 10: Numerical results and exact solution for steady states in channels with rectangular cross-section and width variation: (left) Test C with progressive longitudinal contraction and (right) Test D with progressive longitudinal expansion.

The numerical bed evolution in Case C (Fig. 10-left) shows a bed erosion downstream caused by an increase in the solid transport rate per unit width q_s. On the other hand, the width expansion (Test D) leads to a progressively lower solid discharge q_s, hence the bed level increases downstream (Fig. 10-right). However, the total solid discharge Q_s in the channel remains constant for both cases, indicating that the steady state is reached. Numerical results for the bed level agree perfectly with the exact solution derived from imposing

steady conditions in a rectangular channel of variable width (67). Deduction of this exact solution is detailed in Appendix B. The equilibrium bed slope for prismatic rectangular channels of width 1 m, 0.5 m and 3 m are also depicted in Fig. 10, showing a perfect agreement with those numerically calculated at $x < 20\ m$ and $x > 80\ m$.

$$S_0 = S_f - \frac{1}{3}\frac{h}{B}(Fr^2 + 2)\frac{dB}{dx} \tag{67}$$

4.3. Dam-break with analytical solution

Three test problems with exact solution presented in [32] are reported in this section. The tests are one-dimensional Riemann problem for movable bed, in which the friction shear stress term has been neglected in the momentum equation. Features and initial condition for the three problems are summarized in Table 2. All the simulations were made with CFL = 1, $\Delta x = 0.01\ m$ and sediment layer porosity $p = 0.4$. Results predicted by the CCM model are presented for a final simulation time $t = 2\ s$.

Test	h_L (m)	h_R (m)	u_L (m/s)	u_R (m/s)	ϵ_{bL} (m)	ϵ_{bR} (m)	A_g (dim)
DAS1	2.0	2.0	0.25495	2.3251	3.0	2.846848	0.01
DAS2	2.25	1.18868612	0.2050	2.4322	5.0	5.124685	0.01
DAS3	6.0	5.2	0.30037	15.16725	3.0	4.631165	$0.01/h$

Table 2: Summary of the dam-break test cases with exact solution.

Cases DAS1 and DAS2 prove the performance of the numerical scheme to converge to the exact solution of both Riemann problems. The CCM model correctly reproduces the rarefaction waves involved in these two problems. The contact and shock waves were also captured accurately, in terms of strength and position, for all the conserved variables. Results for cases DAS1 and DAS2 at the final simulation time are depicted in figures 11 and 12 respectively, together with the exact solution for both problems. For a more complex description of the wave structure involved in each problem see [32].

Test DAS3 assumes that the Grass coefficient is not constant but it varies as a function of the water depth. To clarify the influence of the cellwise flux term in the numerical formulation when A_g is not constant through the local Riemann problem, results for DAS3 with the conservative and non-conservative schemes are depicted in figure 13, together with the exact solution for the last simulated time. The CCM model is able to describe properly

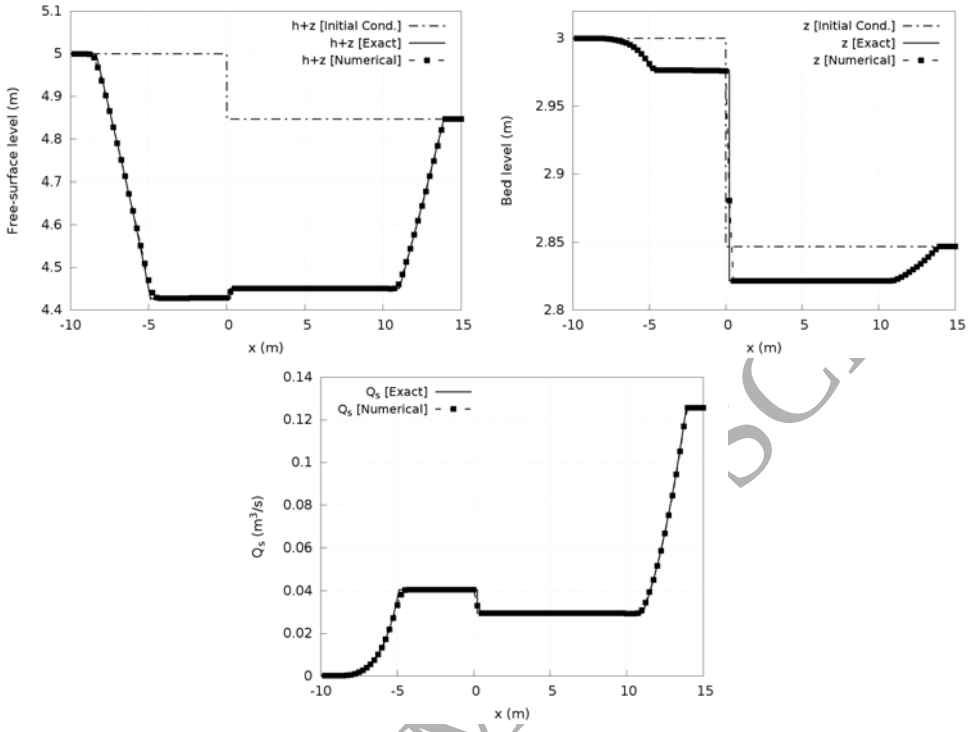

Figure 11: Numerical and exact solution at $t = 2\ s$ for the test case DAS1.

the solution structure for all the conserved variables and all the waves were captured accurately. Furthermore, with the NCCM model the numerical solution degenerates clearly due to the lack of conservation of the solid bed material volume.

4.4. Dam-break over bed step and cross-section change

The aim of this section is to assess the performance of the numerical scheme to deal with transient flow through cross-section shape changes. A dam-break case with $h_L = 2.5\ m$ and $h_R = 0.7\ m$ is simulated over a bed step ($\epsilon_{bL} = 1.5\ m$ and $\epsilon_{bR} = 1.0\ m$) for different cross-section shapes both upstream and downstream. A progressive linear cross-section transition occurs between $x = -1\ m$ and $x = +1\ m$]. Upstream and downstream this transition region, the channel is prismatic, with the cross-sections indicated in Table 3. The discontinuity in the water surface and the bed step are located at $x = 0$.

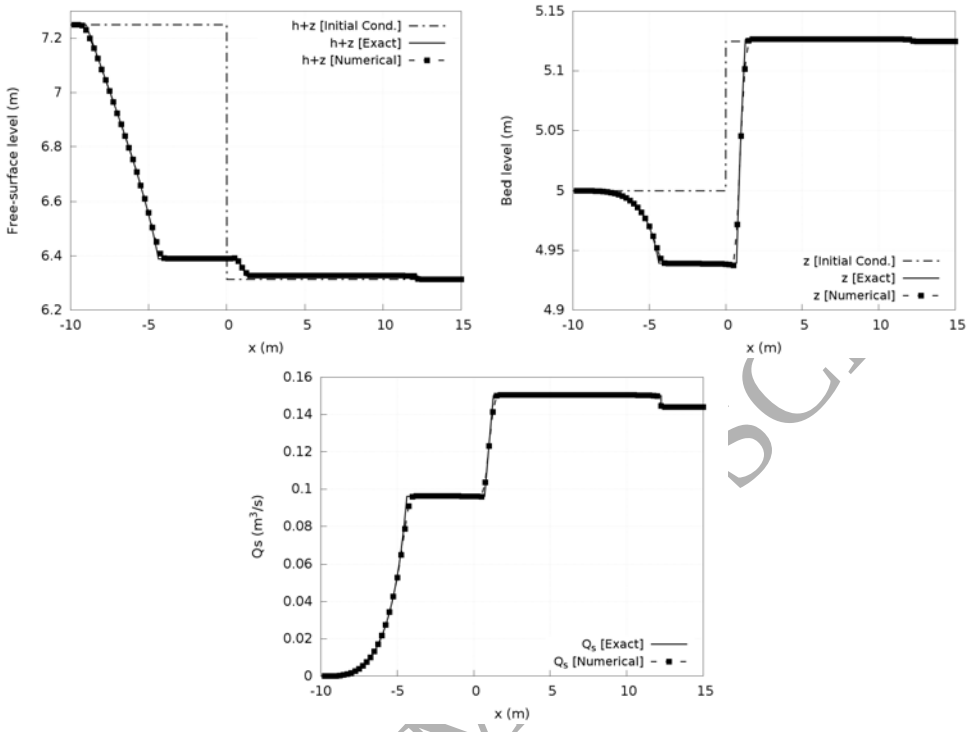

Figure 12: Numerical and exact solution at $t = 2\ s$ for the test case DAS2.

All the cases were simulated with CFL $= 1$, $\Delta x = 0.05\ m$ and sediment layer porosity $p = 0.6$. The Manning coefficient was $n = 0.025 s m^{-1/3}$ and the solid discharge per unit width was estimated by the *Meyer-Peter-Müller* model. The solution was evolved with the horizontal layer erosion-deposition mechanism (Option A) until a final simulation time $t = 3.0\ s$.

The numerical model is able to handle the solid discharge variations caused by sudden expansions and contractions in rectangular channels (Fig. 14). An expansion downstream leads to higher erosion upstream the bed step. On the contrary, a contraction downstream caused a lower erosion upstream the bed step.

Finally, the ability of the scheme to handle cross-section shape changes is evaluated by Test 4 and Test 5. Results for a prismatic rectangular (Test 1) and prismatic trapezoidal (Test 6) channels were selected as reference. Results depicted in Fig. 15 show the influence of the cross-section shape change over the erosion on the bed step, leading to marked differences with

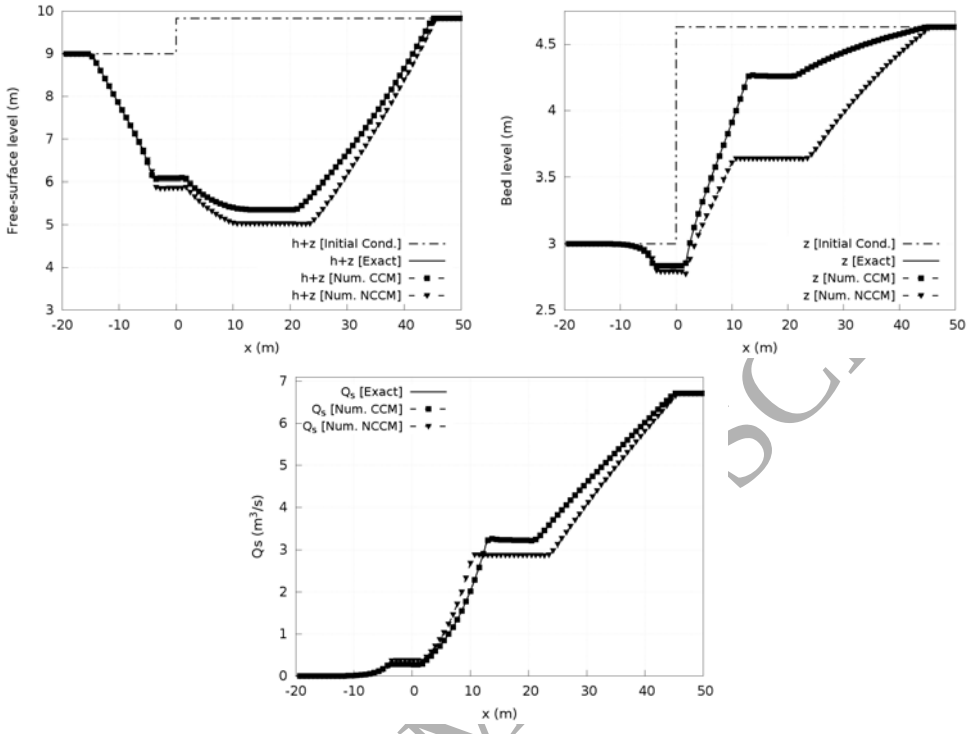

Figure 13: Numerical and exact solution at $t = 2\ s$ for the test case DAS3.

respect to the case in which only the width varies but the shape remains rectangular.

4.5. Experimental dam-break in rectangular channel

The aim of this section is to assess the performance of the CCM model by comparing the obtained numerical results with experimental measurements for a set of laboratory dam-breaks over a sand bed. For these cases, the Grass coefficient is assumed variable and evaluated by an empirical law. The experiments was performed by [54] in a rectangular cross-section flume of 6,3 m length on both sides of a central gate and 25 cm width. The bed was formed by a uniform coarse sand of median diameter $d_m = 1.82\,mm$, density $\rho_s = 2683\,kg/m^3$, friction angle $\varphi = 30°$, negligible cohesion and porosity $p = 0.47$. The Manning roughness coefficient was estimated as $n = 0.0165\,sm^{-1/3}$.

Two different experimental dam-break cases have been reproduced, varying the water depth upstream and downstream the central gate. Table 4

Test	Up-shape	B_b (m)	$tg\psi$	Down-shape	B_b (m)	$tg\psi$	A_g
1	Rectangular	1.0	0	Rectangular	1.0	0	*MPM*
2	Rectangular	1.0	0	Rectangular	1.25	0	*MPM*
3	Rectangular	1.0	0	Rectangular	0.75	0	*MPM*
4	Rectangular	1.0	0	Trapezoidal	1.25	0.2	*MPM*
5	Trapezoidal	1.25	0.2	Rectangular	1.0	0	*MPM*
6	Trapezoidal	1.25	0.2	Trapezoidal	1.25	0.2	*MPM*

Table 3: Summary of the geometrical features for the hypothetical dam-breaks cases.

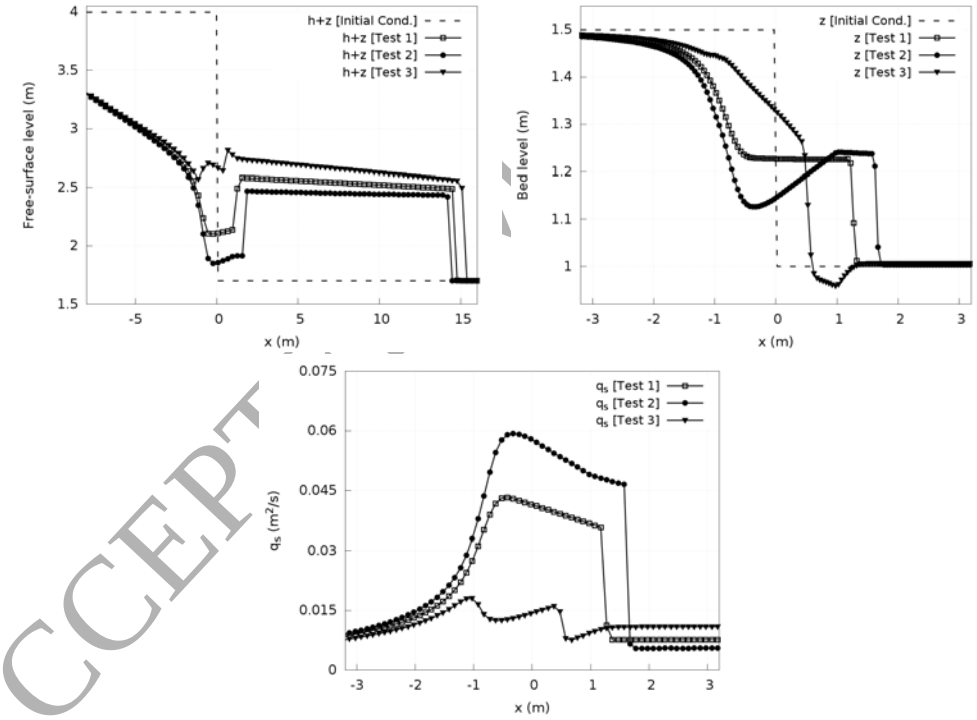

Figure 14: Dam-breaks in rectangular channels with variable width: (top left) free-surface level, (top right) bed level at the transition region and (bottom) solid discharge per unit width q_s.

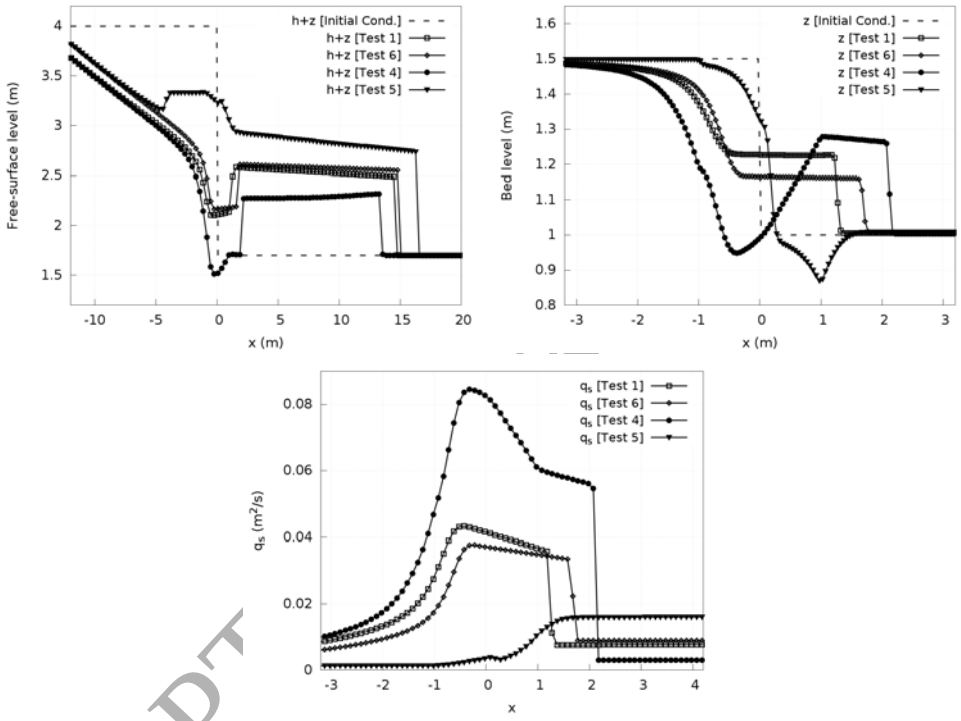

Figure 15: Dam-breaks in channels with cross-section shape changes: (top left) free-surface level, (top right) bed level at the transition region and (bottom) solid discharge per unit width q_s.

shows the features of the simulated dam-breaks. All the simulations were performed with $CFL = 1$ and $\Delta x = 0.01\ m$ and cross-section updating mechanism A. The solid discharge per unit width was approximated by the modified *Smart* formula proposed by [17]. No boundary conditions were imposed at the downstream ending section.

Test	h_L (cm)	h_R (cm)	ϵ_{bL} (cm)	ϵ_{bR} (cm)	A_g
ED1	25	10	10	0	*Smart CFBS*
ED2	25	0	10	0	*Smart CFBS*

Table 4: Summary of the experimental dam-break tests. Null value for the bed layer thickness indicates the reference level.

Experimental and numerical results for the two cases ED1 and ED2 at times $t = 0.5\ s$, $t = 1.0\ s$ and $t = 1.5\ s$ are plotted in Fig. 16 and 17. The computed bed level evolves correctly for the two cases and with the same velocity observed in the experiments. Furthermore, the free-surface level is also reasonably well predicted, event at the first stages after the gate opening, and the progress of the dam-break shock wave agrees with the measured data, regardless of dry or wet condition downstream the central gate.

Finally, it is worth noting that this is a widely extended benchmark case which has been used to test other 1D numerical models reported in literature, most of them fail to predict the earliest stages after the gate opening [24]. Moreover, the bed and free surfaces computed by the presented coupled model did not show the numerical oscillations which are common with uncoupled models for this test case, demonstrating the stability and robustness of the numerical scheme.

4.6. Experimental dam-break with cross-section degradation

An idealized experimental dam-break over a partially erodible bed was carried out at the Civil Engineering Laboratory of the UCL (Louvain, Belgium) [55]. A channel $0.495\,m$ wide and $5.68\,m$ long was divided in half by a gate and connected with an upstream reservoir ($2.44 \times 2.39\,m$). Downstream the gate ($2.92\,m$ long), an uniform erodible material was set with a semi-trapezoidal cross-section. The bed thickness was $8\,cm$ above the non-erodible channel floor and the bank crosswise slope was 50°. There was no slope along the longitudinal direction. Upstream the gate ($2.76\,m$ long) a

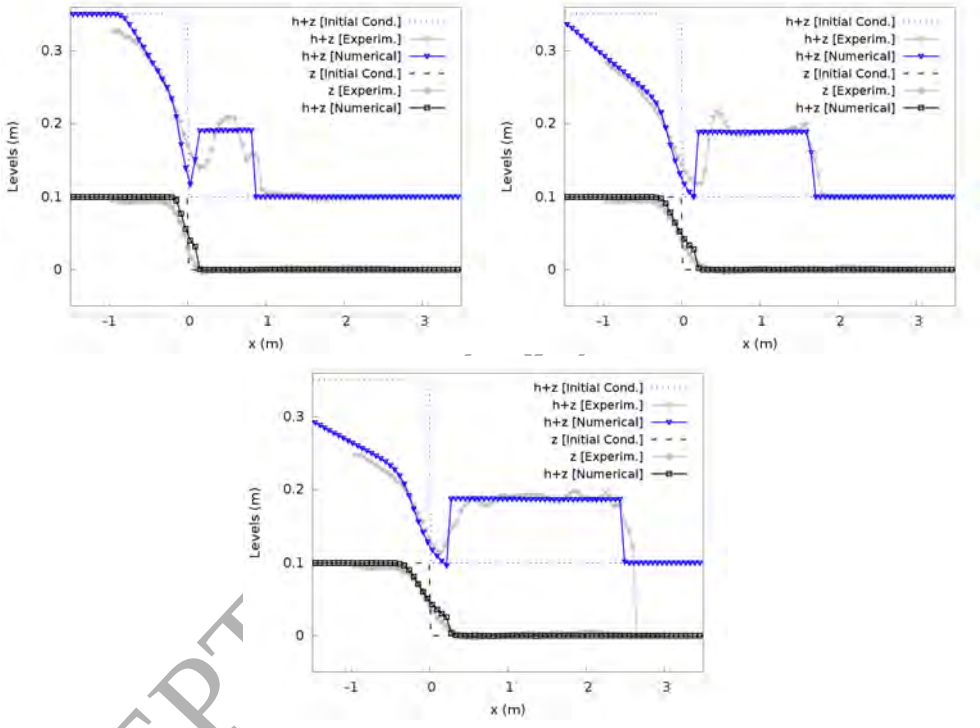

Figure 16: Measured and computed free-surface and bed levels for case ED1 at (top left) $t = 0.5\ s$, (top right) $t = 1.0\ s$ and (bottom) $t = 1.5\ s$.

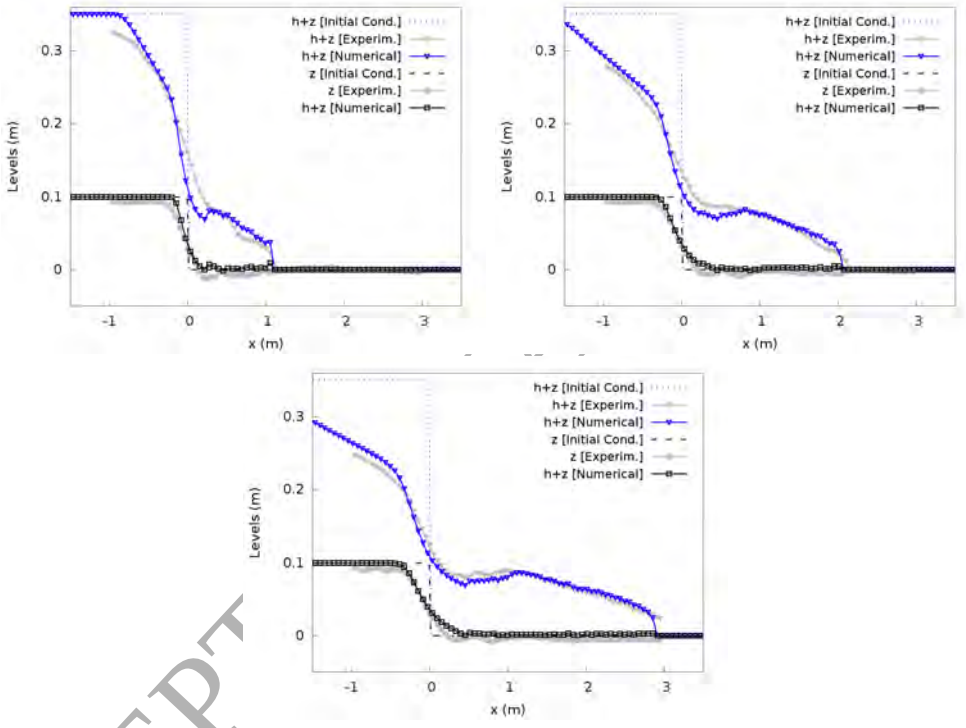

Figure 17: Measured and computed free-surface and bed levels for case ED2 at (top left) $t = 0.5\ s$, (top right) $t = 1.0\ s$ and (bottom) $t = 1.5\ s$.

rigid bank with the same cross-section as the erodible reach was set to minimize two-dimensional flow phenomena. A scheme of the experimental setup is shown in Fig. 18. The erodible material was a coarse uniform sand of median diameter $d_m = 1.8\,mm$, a density $\rho = 2615\,kg/m^3$, and a bed porosity $p = 0.405$.

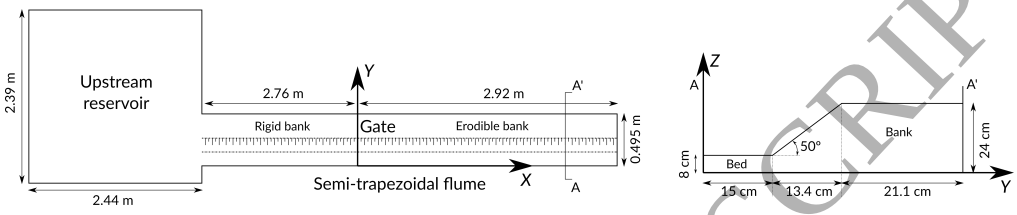

Figure 18: Sketch of the experimental setup [55]: (left) top view and (right) section A-A'.

An initial water depth $h_0 = 15\,cm$ above the bed was set upstream the gate. Downstream the gate, the bed material was initially saturated. Then the gate was suddenly open, releasing a dam-break wave which rapidly propagated along the erodible reach. The highly erosive flow attacked the toe of the bank, triggering a series of intermittent bank failures. Thus, the destabilized material was transported downstream by the flow. The erodible bed evolution was measured at different cross-sections downstream the gate by a laser-sheet imaging technique. Approximately 10 seconds after the gate opening most of the morphological change had occurred, although experimental measurements were reported until 15 seconds after the wave releasing.

This is a challenging benchmark test for 1D erosive models since marked two-dimensional flow phenomena occur in the near-field of the gate. Moreover, the occurrence of bank failure forces to incorporate a mechanism in the numerical scheme to reproduce properly the embankment stability. Therefore, a conservative numerical procedure is introduced in the cross-section updating step of the numerical scheme to correctly predict the bank failures. A dynamic stability angle of 28° is estimated for the cross-section submerged bed. A Manning's roughness coefficient $n = 0.016\,sm^{-1/3}$ is estimated for the erodible material by means of the Strickler formula $n = \frac{1}{21.1} d_{50}^{1/6}$ (Strickler, 1932). The Manning's coefficient of the flume rigid material is also set to $n = 0.01\,sm^{-1/3}$. The domain is discretized in 525 cells in the longitudinal direction, with a variable cell size δx which was minimum at the near-field of the gate ($\delta x_{min} = 2\,mm$), and 101 panels at the cross direction with constant

panel size ($\delta y = 5\,mm$).

Fig. 19 depicts the two-dimensional map of erosion-deposition patterns downstream the gate at $t = 10\,s$ for three different experimental closure transport rate relations and cross-section updating mechanism B. Erosion zones are marked with warm colors, whereas deposition is represented by cold colors. The erosion-deposition distribution is quite similar for MPM and Nielsen transport rates, with a sediment accumulation at the toe of the bank caused by the stability failures. The highest erosion is predicted at the embankment head, whereas slight erosion occurs at the channel bed. With the Smart-CFBS formulation some differences can be appreciated but the global erosion-deposition distribution follows the same pattern as with the previous closure relations.

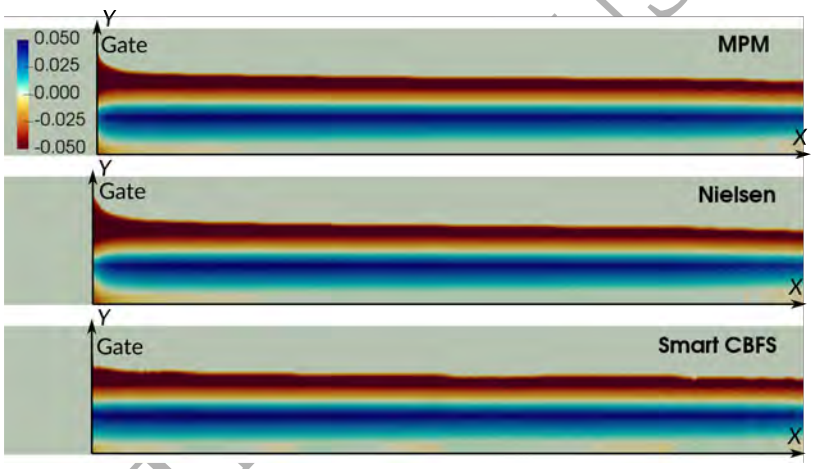

Figure 19: 2D map of erosion-deposition patterns with cross-section updating mechanism B and Meyer-Peter-Müller, Nielsen and Smart-CFBS transport rate formula for $t = 10.0\ s$.

Furthermore, the experimental cross-section evolution at $x = 0.25\,m$, $x = 0.50\,m$, $x = 0.95\,m$ and $x = 1.50\,m$ downstream the gate is shown for five different times after the gate opening in Fig. 20 ($t = 1\,s$, $t = 3\,s$, $t = 5\,s$) and Fig. 21 (($t = 10\,s$, $t = 15\,s$). The predicted cross-sections at the same instants are also plotted for the Nielsen closure relation and cross-section updating mechanisms B (uniform) and C (stress weighted erosion and deposition). Moreover, two-dimensional fields of erosion-deposition patterns (Nielsen with mechanism B) are also depicted for each time.

The highest differences between computed and measured elevations can

be observed in the near-field of the gate (profile $x = 0.25\,m$) for the first moments after the gate opening ($t = 1\,s$, $t = 3\,s$). The dam-break wave attacks the toe of the bank close to the gate, the bank fails and big portions of the embankment are incorporated to the submerged channel bed. Upstream the gate, the bank is rigid and hence it can not be eroded by the flow, leading to the appearance of a marked two-dimensional flow close to the gate which contributes to increase the bank erosion. As the dam-break wave progresses, the flow becomes more one-dimensional and the measured and computed bed elevations start to show a better agreement.

Despite this 2D phenomenon close to the gate, experimental and predicted cross-section profiles generally show a good agreement, especially with the simulations performed with the updating mechanism B (uniform erosion-deposition). The mechanism C (stress weighted erosion-deposition) tends to overestimate the material removed from erodible bed in the near-field of the gate (see especially the profile $x = 0.25\,m$ close to the vertical flume side). On the other hand, both erosion-deposition options offer quite similar results for the embankment regions, suggesting that the bank failure phenomena controlled the cross-section degradation at these regions.

4.7. Dyke-break wave in the River Ha!Ha! (1996)

The aim of this numerical case is to test the model performance against a real-scale high-erosive flow. In 1996 (July 19–21), the River Ha!Ha! (Quebec, Canada) underwent large morphological changes due to the failure of a secondary earth dyke in the Lake Ha!Ha!. The water level overtopped the dyke head, eroded a new channel to the river thalweg and caused the lake drainage. The free-surface level in the lake dropped from $381\,m$ AMSL to $370\,m$ AMSL in 72 hours and released a drainage hydrograph with a peak discharge around $1000\,m^3/s$. The flood wave progressed along the Ha!Ha! valley ($36\,Km$) until it reached the Ha!Ha! Bay. Fig. 22 shows a general sketch of the Ha!Ha! valley, extracted from [56].

The river bed resulted largely modified by the flood event from the lake to the river mouth [57, 58]. High erosion patterns were observed downstream the dyke (PK0-PK2.5), at the 'Chute-à-Perron' reach (PK20-PK23.5) and downstream the 'Rocheux-et-d'Hamel' tributary ('Lower Canyon' reach, PK28-PK32). Marked sediment accumulation was observed at the 'Eaux-mortes' reach (PK23.5-PK27), where the material eroded in 'Chute-à-Perron' was partially deposed. Finally, channel widening was observed in the near reach to the river mouth (PK32-PK36). This is a widely extended morphodynamic

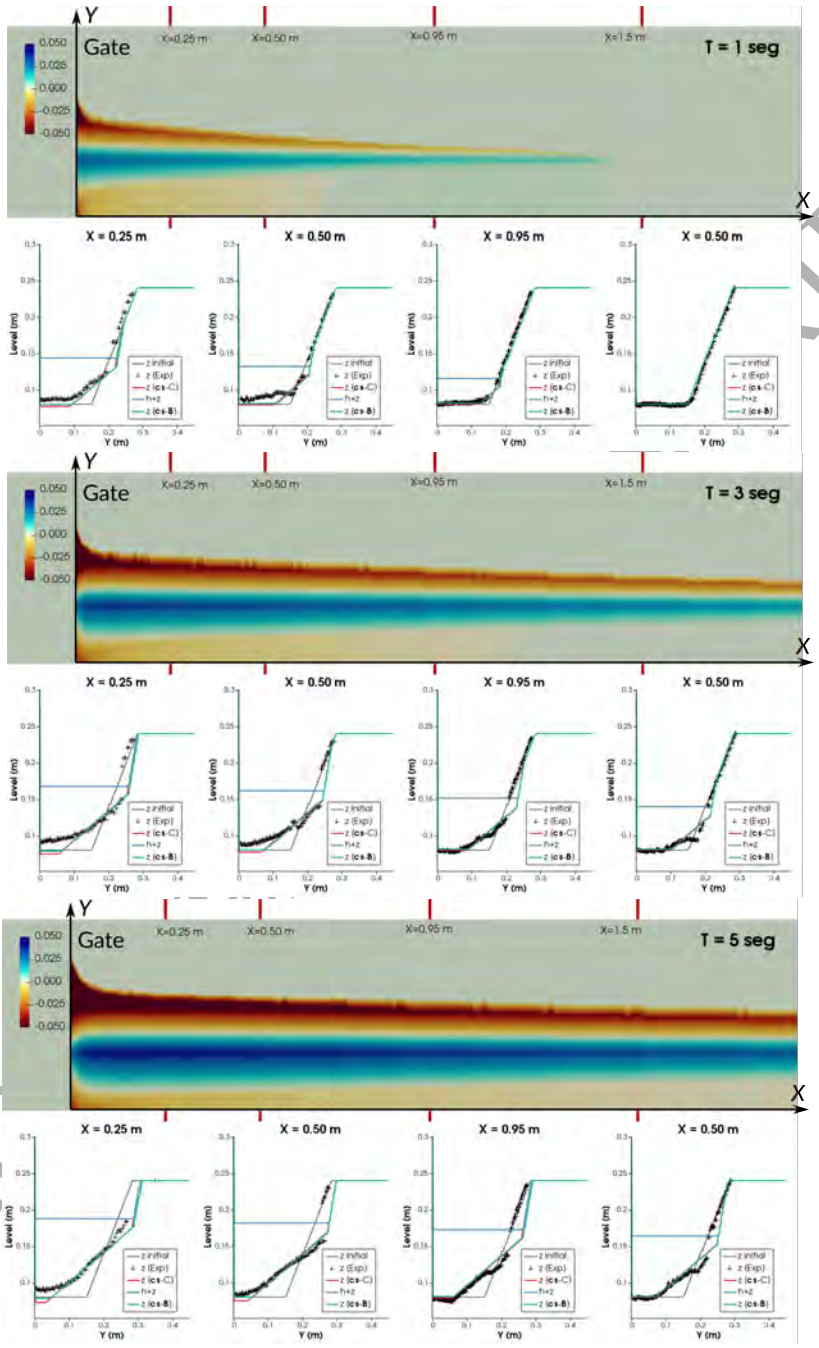

Figure 20: Map of erosion-deposition patterns and comparison of measured and predicted cross-sectional profiles for $t = 1.0\ s$, $t = 3.0\ s$ and $t = 5.0\ s$.

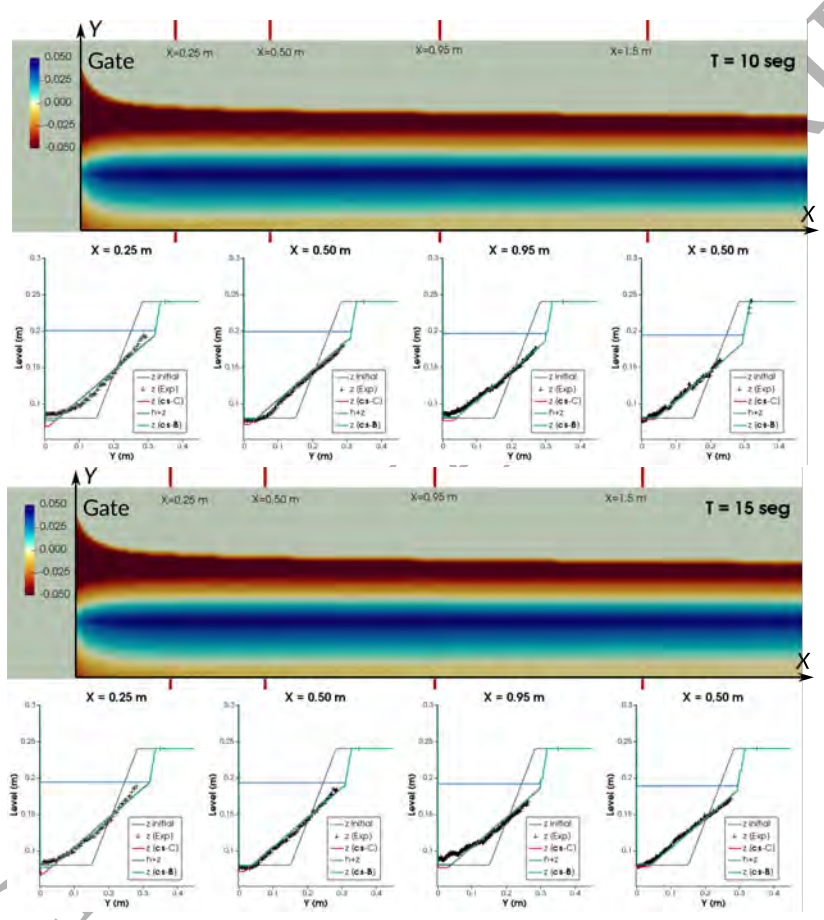

Figure 21: Map of erosion-deposition patterns and comparison of measured and predicted cross-sectional profiles for $t = 10.0\ s$ and $t = 15.0\ s$.

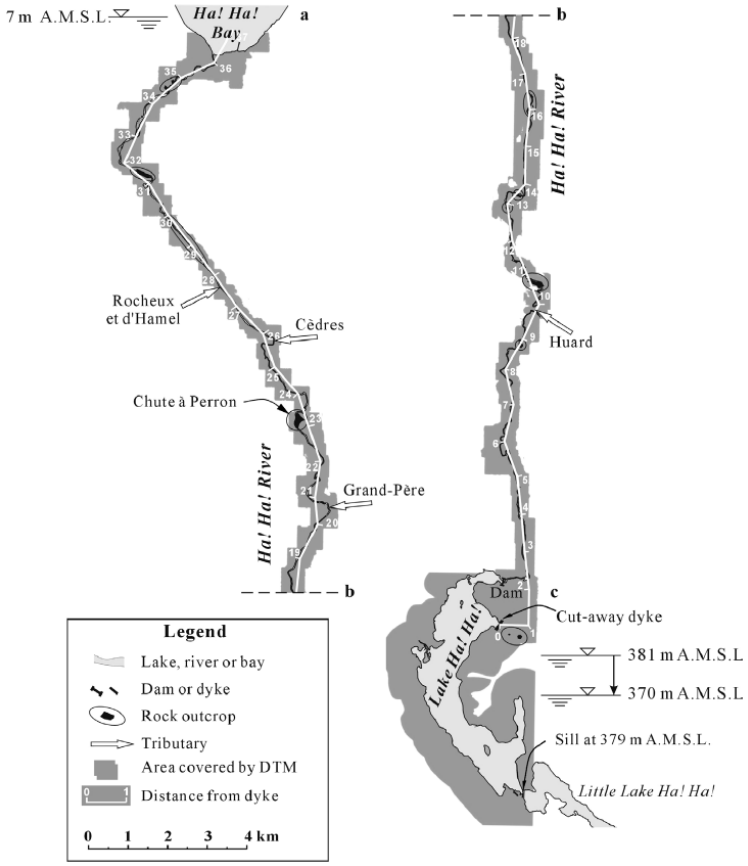

Figure 22: Ha!Ha! valley sketch, extracted from [56].

benchmarking test, initally proposed by [59]. A complete description of the case, including hydrological data and a detailed topography characterization pre- (1994) and post-flood (1996) were reported by [56]. Moreover, previous numerical studies of this benchmarking test using 1D morphodynamical models have been reported by [11, 24, 39, 60–62].

Field observations showed that both soft sand and gravel, as well as bedrock, were exposed along the valley. [60] characterized the non-cohesive material of the riverbed downstream the dyke: median diameter $d_{50} = 0.5\,mm$ with standard deviation $2.7\,mm$, density $\rho_s = 2650\,kg/m^3$, porosity $p = 0.4$ and internal friction angle 35°. These values have been retained for the whole domain since additional information does not exist. [11] adopted a smaller diameter ($0.1\,mm$) for the sediment acumulation in the 'Chute-à-Perron' reach. Location of the exposed outcrops were identified in [57, 58] and a complete reconstruction of the bedrock elevation was provided in [56]. The inlet hydrograph condition was reconstructed from the lake level and area drops [57, 59] and showed a peak discharge of $910\,m^3/s$ (Fig. 23). A null sediment discharge condition was also imposed at the inlet section. For the downstream outlet condition, the water level at the Ha!Ha! Bay was set to a constant value of $7\,m$ AMSL. A global value for the Manning's roughness coefficient in Ha!Ha! valley was estimated between $0.036\,sm^{-1/3}$ to $0.043\,sm^{-1/3}$ [58]. However, [11, 24] adopted a global value $n = 0.067\,sm^{-1/3}$, more appropriate for domains with vegetation, obstructions and exposed bedrock. This friction coefficient value is retained for the outcrop regions, regardless of the global Manning's coefficient adopted for the whole domain. The initial conditions were estimated by the previous simulation of the fixed-bed steady state along the river with a constant inlet discharge of $35\,m^3/s$, following [61].

Twelve different simulation setup were tested. The main parameters are summarized in Table 5:

In order to obtain a quantitative comparison of the different setups, the domain is divided into seven reaches, depending on the characteristic bed evolution observed after the flood:

1. Reach 1 (Cut-away dyke), from PK0 to PK2.5: Erosion of a new channel.
2. Reach 2 (Upper Boilleau), from PK2.5 to PK8: Aggradation in the valley bottom.
3. Reach 3 (Lower Boilleau), from PK8 to PK20: Slight riverbed erosion.

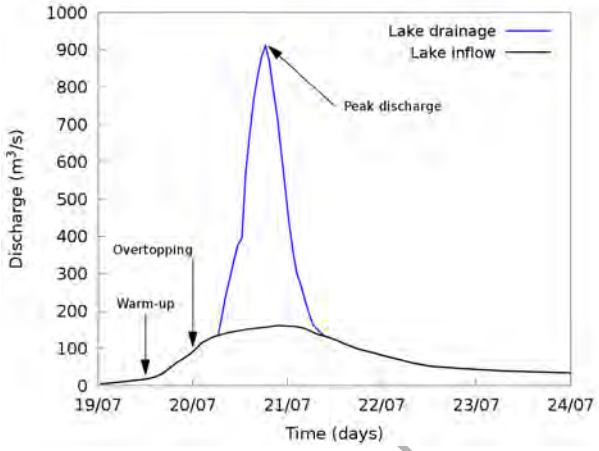

Figure 23: Inlet hydrograph [57].

Run	A_g	d_{50} (mm)	n $(sm^{-1/3})$	Mech. (Ero-Dep)
R1	*MPM*	0.5	0.036 (1) - 0.067 (2)	**A** (Uniform-Layers)
R2	*MPM*	0.5	0.036 (1) - 0.067 (2)	**B** (Uniform-Uniform)
R3	*MPM*	0.5	0.036 (1) - 0.067 (2)	**C** (Weighted-Weighted)
R4	*Smart-CBFS*	0.5	0.036 (1) - 0.067 (2)	**A** (Uniform-Layers)
R5	*Smart-CBFS*	0.5	0.036 (1) - 0.067 (2)	**B** (Uniform-Uniform)
R6	*Smart-CBFS*	0.5	0.036 (1) - 0.067 (2)	**C** (Weighted-Weighted)

Table 5: Summary of simulation setup for the twelve runs tested.

4. Reach 4 (Chute-à-Perron), from PK20 to PK23.5: Severe erosion of the valley.
5. Reach 5 (Eaux-mortes), from PK23.5 to PK28: Aggradation in the riverbed.
6. Reach 6 (Lower Canyon), from PK28 to PK32: Moderate bed erosion.
7. Reach 7 (River mouth), from PK28 to PK36.5: Major widening and deepening of the channel.

The thalweg elevation (lowest point at each cross-section) profile along the river valley before and after the dyke breaking were extracted from the 2D DTM field data. Moreover, estimations of the maximum water levels reached during the flood at 42 point downstream the dyke were performed by the INRS-Eau in 1997. These estimations were based on surveys of the valley residents and field assessment of the local high water marks.

In order to estimate the performance of the model, the BSS index (Brier Skill Score) [63] for the thalweg elevation and the high water marks is computed for each reach separately. The BSS index have been used as a criteria to determine the performance of morphodynamic numerical models in complex real field applications [63, 64]. Comparison of the model results is made against a baseline prediction, which in this work is assumed to be the initial bed topography. Then, the BSS index is calculated as:

$$BSS = 1 - \frac{\sum_{i=1}^{N}(z(x_i, t_{end})_{meas} - z(x_i, t_{end})_{sim})^2}{\sum_{i=1}^{N}(z(x_i, t_{end})_{meas} - z(x_i, 0)_{sim})^2} \tag{68}$$

being $z(x_i, t_{end})_{meas}$ and $z(x_i, t_{end})_{sim}$ the observed and predicted data in the point i at final time, respectively; $z(x_i, 0)$ the initial data at the point i and N the number of measurements. Reasonable agreement between field data and predicted results is considered for BSS values 0.3-0.6, whereas BSS values above 0.6 indicate good agreement [64]. On the other hand, BSS values below 0.3 are obtained for poor fit with the observed data.

Table 6 shows the two best BSS results for the thalweg elevation obtained in each reach and the corresponding simulation setup. In general, simulations with the cross-section updating mechanism C (stress weighted erosion and deposition) perform better than with the other two option considered. The best thalweg BSS values are obtained for simulations performed with erosion-deposition mechanism type C in four of the seven considered reaches

(1:Cut-away dyke, 2:Upper Boilleau, 4:Chute-à-Perron and 6:Lower Canyon), whereas a simulation sets up with the cross-section updating procedure A offers the best BSS value in the reach 5:Eaux-mortes. Furthermore, simulations set up with a global Manning's coefficient $n = 0.036\, sm^{-1/3}$ offer a better fit with the thalweg elevation field data than simulations with a higher roughness value, with the exception of reach 6:Lower Canyon. Concerning the transport rate closure relation, *Smart-CBFS* formulation seems to offer a better agreement in the upper valley, whereas the *MPM* relation performs better in the near field of reach 4:Chute-à-Perron, where a high erosion was observed. However, all the simulations result in poor BSS values in the reaches 3:Lower Boilleau and 7:River mouth, where an important channel widening was observed.

	Reach 1	Reach 2	Reach 3	Reach 4	Reach 5	Reach 6	Reach 7
1^{st} BSS	0.561955	0.45103	<0.1	0.651193	0.558781	0.855746	<0.1
	R6-1	R6-1	-	R3-1	R1-1	R6-2	-
2^{nd} BSS	0.527114	0.418707	<0.1	0.581139	0.519807	0.807235	<0.1
	R6-2	R6-2	-	R3-2	R1-2	R5-2	-

Table 6: Summary of the maximum BSS values obtained for each reach.

Fig. 24 shows a comparison of the thalweg elevation computed with the three different options considered for the erosion-deposition mechanism (A, B and C) in the reaches 4 and 6, where the highest erosive events were observed. The depicted results were obtained using *Smart-CFBS* formulation and the Manning's coefficient $n = 0.036\, sm^{-1/3}$ for the reach 4:Chute-à-Perron (R1-1, R2-1 and R3-1), and with *MPM* and $n = 0.067\, sm^{-1/3}$ for the reach 6:Lower Canyon, corresponding to the best setup for each reach (see Table 6). Cross-section updating configuration type C offers the best result at these high-eroded reaches for the thalweg elevation profile. However, although the bed evolution trends are reasonably well predicted, important quantitative differences can be found in the incision created by the flood in the river valley along the reach 4:Chute-à-Perron.

Regarding the high water marks predicted by the numerical model, the computed results were interpolated to the experimental data locations. In Table 7 the mean absolute difference between observed high marks and the predicted ones at the same location have been tabulated for all the simula-

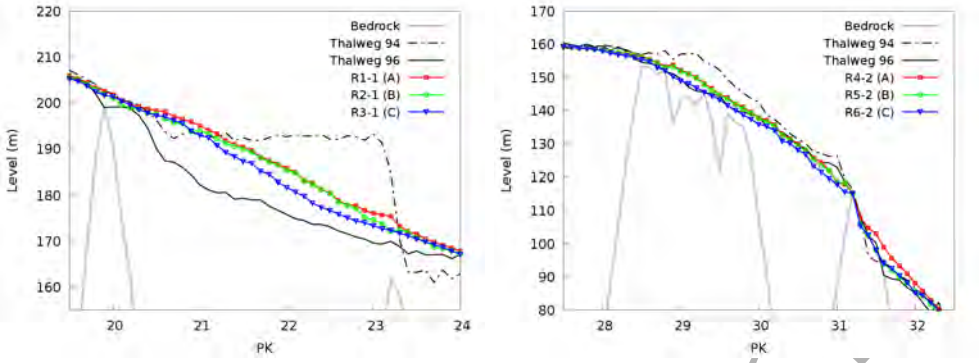

Figure 24: Thalweg elevation profiles in (left) reach 4:Chute-à-Perron and (right) 6:Lower Canyon. Simulation were performed with: (left) *Smart-CFBS* and $n = 0.036\, sm^{-1/3}$; (right) *MPM* and $n = 0.067\, sm^{-1/3}$.

tion setups. A better agreement is obtained in simulations with Manning's roughness coefficient $n = 0.067\, sm^{-1/3}$ (mean deviation $\approx 0.40\, m$) than in those with $n = 0.036\, sm^{-1/3}$ (mean deviation $\approx 1.5\, m$), although it is worth mentioning that the observed data error was assessed around 2 m and hence both values can be considered reasonably fair.

Run	**1** ($n = 0.036$)	**2** ($n = 0.067$)	**Run**	**1** ($n = 0.036$)	**2** ($n = 0.067$)
R1	1.60	0.45	**R4**	1.49	0.35
R2	1.64	0.40	**R5**	1.50	0.38
R3	1.69	0.66	**R6**	1.52	0.36

Table 7: Mean absolute difference between observed high water marks and predicted maximum water levels for all the simulation setups tested.

Furthermore, the most remarkable absolute differences for the maximum levels reached by the dyke-break wave along the river valley tend to appear in the last reach (7:River mouth), as well as in the reach 4:Chute-à-Perron because of the large deviations on the predicted thalweg. Nevertheless, the maximum absolute difference always remains below 8 meters (Fig. 25). The most remarkable trend which can be observed along the river valley is that simulations performed with the lowest Manning's coefficient (1) offered underestimated maximum water levels, whereas using a higher Manning's coefficient leads to predicted maximum water levels above those were observed.

Finally, Figures 26 and 27 show the observed riverbed evolution at seven

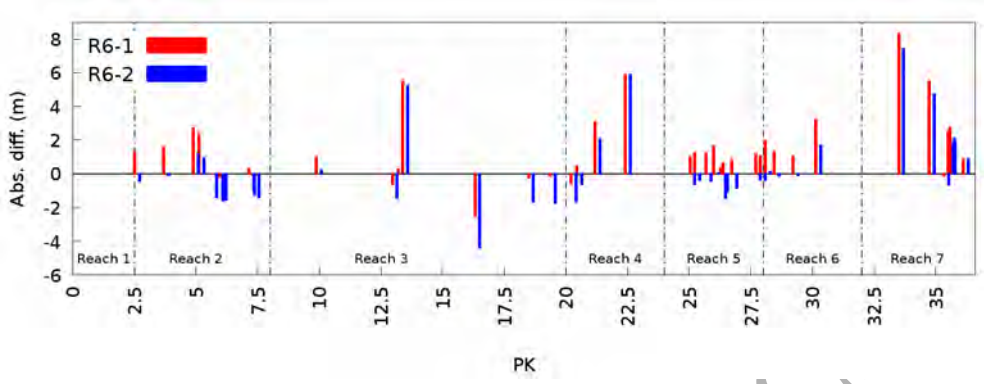

Figure 25: Absolute difference between observed high water marks and numerical maximum levels predicted along the Ha!Ha! valley for simulations R6-1 and R6-2.

different cross-section (one in each reach) which are representative of the erosion-deposition behavior caused by the flood. Results of the simulations R4-2, R5-2 and R6-2 are also depicted in order to show the influence of the cross-section updating mechanism in the riverbed shape evolution. All the numerical profiles were obtained with the *Smart-CBFS* transport rate relation and $n = 0.067\, sm^{-1/3}$.

Downstream the dyke (reach 1), the model is able to predict reasonably well the excavation of the new channel, regardless of the cross-section updating option (see Fig. 26). Erosion-deposition configurations A and B lead to wider channels, whereas option C causes a deeper incision in the valley floodplains. In reach 2 the influence of the erosion deposition option is less marked and the model predicted the river bed aggradation with an acceptable accuracy. Reach 3 is one of the most challenging due to the complex topography and the presence of various outcrops where the bedrock was exposed. The dyke-break wave caused a slight general erosion in this reach of the Ha!Ha! valley, limited by the presence of the outcrops. Following the BSS criteria, the model fails in this reach, regardless of the simulation setup selected. Nevertheless, global thalweg elevation along the reach and the predicted maximum water levels do not deviate excessively from the ones observed.

Reach 4 was one of the most modified by the flood. A new channel was excavated in the fine sediment of the flood plains creating a high erosive phenomenon which is difficult to capture for one-dimensional morphodynamical

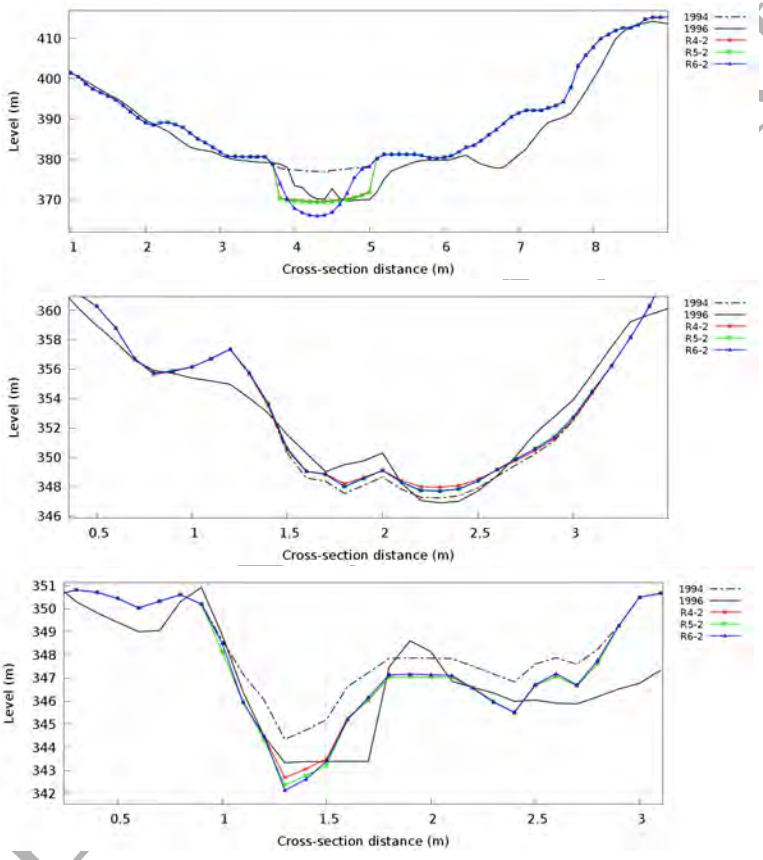

Figure 26: Observed and predicted cross-section evolution at (top) PK0.1 - reach 1:Cut-away dyke, (center) PK3.8 - reach 2:Upper Boilleau and (bottom) PK8.3 - reach 3: Lower Boilleau.

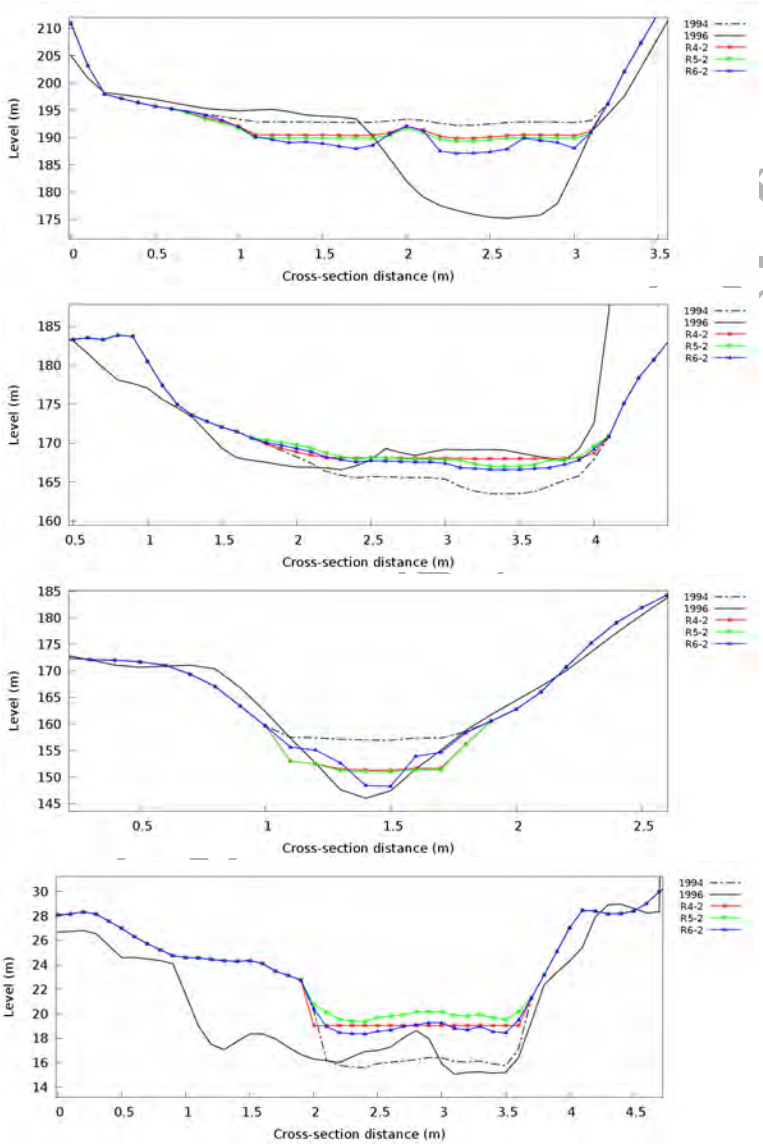

Figure 27: Observed and predicted cross-section evolution at (first row) PK22.1 - reach 4:Chute-à-Perron, (second row) PK23.6 - reach 5:Eaux-mortes and (third row) PK29.1 - reach 6: Lower canyon and (fourth row) PK35.3 - reach 7:River mouth.

models. However, the presented coupled model is able to predict the erosion-deposition trends along the reach with an acceptable accuracy. Nevertheless, the simulated thalweg elevations remain higher than those measured after the flood (see 27). Most of the sediment eroded from the upstream reach were deposited in reach 5, leading to the riverbed aggradation which is well captured by the model. In reach 6 moderate-high erosion was observed after the flood and some bedrock region were exposed creating news outcrops. The numerical results in this reach show a good agreement with the field data, regardless of the selected simulation setup. Near the river mouth (reach 7), a strongly channel widening phenomena dominated the riverbed evolution. The model is not able to capture this widening in a proper way (regardless of the simulation setup) and predicts the cross-section aggradation in order to achieve a higher active width.

Finally, it is worth mentioning that all the simulations have been performed with a CFL = 0.5, leading to a minimum time step of 2.5 sec approximately and guarantying fluid and solid mass conservation. [11] reported numerical stability problems in this benchmarking test for a similar Courant number, therefore the model has demonstrated to offer enough robustness to perform real-scale field cases.

5. Conclusions

A new finite volume scheme has been proposed for the coupled system of shallow water and Exner equations which is applicable to 1D channels with arbitrary geometry. This allows the model to be applied to complex topography domains, such as rivers. The equations have been treated to deal with cross-section shape variations by distinguishing the intercell conservative fluxes due to geometry variations from that caused by the flow features. The resulting coupled system of equations has been rewritten as a non-conservative hyperbolic system with three non-linear characteristic fields. Three different cross-section updating mechanisms have been proposed to evaluate the cross-section shape evolution in non-rectangular channels. The influence of the selected mechanism in the morpho-hydrodynamical coupled system solution is incorporated into the mathematical model by means of a new geometrical parameter c_b which considers the bottom change celerity depending on the solid area temporal evolution. An upwind augmented Roe's scheme has been formulated, including the solid discharge evaluated by both the Grass law and other empirical closure relations. Moreover, numerical

fixes have been proposed to avoid unphysical negative wetted areas and to ensure entropy-preserving approximate solutions in case of transitions fixed-movable bed condition. The proposed scheme emphasizes the necessity of well formulated approximate eigenvalues to ensure positivity and numerical stability in all situations with dynamical time step control solely based on the CFL condition.

Firstly, the proposed scheme has been validated against analytical solutions for both erosive steady flows including width variations and for dam-break over movable bed in rectangular channels. Also the numerical scheme behavior has been compared for hypothetical unsteady cases consisting of dam-break flows in channels with shape variations. Numerical results show that the scheme is able to describe properly the exact solution structure for the conserved variables in all the cases tested. Furthermore, we remark that the ability of the model to handle cross-section shape changes is also proved. The importance of the selected cross-section updating mechanism has also been analyzed, since it determines not only the uncoupled solid area distribution at the cross-section but also the waves celerity of the morpho-hydrodynamical system.

For a more advanced evaluation, the model has also been tested against two set of laboratory unsteady benchmarking erosive cases. They consist of dambreak flows over erodible bed involving a bed step and cross-section degradation respectively. In the first one, the proposed model demonstrates its capability to deal with highly erosive unsteady flow, being able to predict the bed elevation and free surface position reasonably well, even for the first stages after the gate opening. In the second laboratory benchmarking test, the coupled scheme is able to correctly estimate the cross-section changes produced in trapezoidal erodible channel by a dam-break flow. The numerical results for both laboratory experiments show a good agreement with the measured data that can be considered better than the results that other 1D models obtain for these empirical tests.

Finally, the proposed coupled model has been faced to a real-scale field case. Simulating the 1996 flood in the Ha!Ha! river is one of the most challenging benchmarking tests for 1D erosive models. The Ha!Ha! flood case involves a complex bed bathymetry with high gradients, bed rock chutes and very irregular cross-sections, a highly variable discharge inlet condition and considerably fast changes in the bed elevation with new main channel appearance. Therefore, one of the demanded features to reproduce this test case is the ability of the numerical scheme to deal with abrupt cross-section changes

and to adapt to different flow regimes. Despite the intrinsic limitations of 1D models to properly predict secondary flows in complex cross-sections, as the Ha!Ha! river, the numerical results computed with the proposed model shows a fairly acceptable agreement with the bed variation field data in most of the river reaches. The dike breaking and the thalweg evolution in highly eroded reaches are well approximated. Nevertheless, important discrepancies appear in the reaches involving low deposition rates in compound cross-section and channel widening, especially at the low valley reaches. The predicted morphological adjustment of the river in response to the upstream discharge boundary condition depends strongly on the mechanism chosen to update the cross-section and on the empirical closure relation for the solid transport rate determination. The stress-weighted mechanism proposed in this work seems to offer the most accurate results, although probably using a more complex method to compute the local boundary shear stress at the cross-section can lead to improve the numerical predictions of the model. However, as concluding remark, it is worthy of mention that the proposed numerical discretization of the coupled Shallow water-Exner model demonstrates a good performance, efficiency and robustness for this extremely complex case, where previous works of other authors reported numerical stability problems in presence of time steps of the same size as those used in this work.

Acknowledgements

This work was partially funded by the MINECO/FEDER under research project CGL2015-66114-R and by Diputacion General de Aragon, DGA, through Fondo Europeo de Desarrollo Regional, FEDER.

References

References

[1] W. Wu, Computational River Dynamics, NetLibrary, Inc, CRC Press, 2007.

[2] D. Lyn, M. Altinakar, St. Venant-Exner equations for near-critical and transcritical flows, Journal of Hydraulic Engineering 128 (6) (2002) 579–587.

[3] L. Goutière, S. Soares-Frazão, C. Savary, T. Laraichi, Y. Zech, One-Dimensional model for transient flows involving bed-load sediment transport and changes in flow regimes, Journal of Hydraulic Engineering 134 (6) (2008) 726–735.

[4] M. Castro-Díaz, E. Fernández-Nieto, A. Ferreiro, Sediment transport models in shallow water equations and numerical approach by high order finite volume methods, Computers & Fluids 37 (3) (2008) 299 – 316.

[5] F. Benkhaldoun, S. Sari, M. Seaid, A flux-limiter method for dam-break flows over erodible sediment beds, Applied Mathematical Modelling 36 (10) (2012) 4847 – 4861.

[6] C. Juez, J. Murillo, P. García-Navarro, A 2d weakly-coupled and efficient numerical model for transient shallow flow and movable bed, Advances in Water Resources 71 (2014) 93 – 109.

[7] F. Charru, Selection of the ripple length on a granular bed sheared by a liquid flow, Physics of Fluids 18 (12) (2006) 121508.

[8] A. Armanini, G. Di Silvio, A one-dimensional model for the transport of a sediment mixture in non-equilibrium conditions, Journal of Hydraulic Research 26 (3) (1988) 275–292.

[9] W. Wu, D. Vieira, S. Wang, One-dimensional numerical model for nonuniform sediment transport under unsteady flows in channel networks, Journal of Hydraulic Engineering 130 (9) (2004) 914–923.

[10] W. Wu, S. Wang, One-dimensional modeling of dam-break flow over movable beds, Journal of Hydraulic Engineering 133 (1) (2007) 48–58.

[11] K. El Kadi Abderrezzak, A. Paquier, One-dimensional numerical modeling of sediment transport and bed deformation in open channels, Water Resources Research 45 (5).

[12] D. Furbish, P. Haff, J. Roseberry, M. Schmeeckle, A probabilistic description of the bed load sediment flux: 1. theory, Journal of Geophysical Research: Earth Surface 117 F03031.

[13] P. Hu, Z. Cao, G. Pender, H.-H. Liu, Numerical modelling of riverbed grain size stratigraphic evolution, International Journal of Sediment Research 29 (3) (2014) 329 – 343.

[14] Z. Cao, Z. Li, G. Pender, P. Hu, Non-capacity or capacity model for fluvial sediment transport, Proceedings of the Institution of Civil Engineers - Water Management 165 (4) (2012) 193–211.

[15] Z. Cao, P. Hu, H.-H. Pender, G. Liu, Non-capacity transport of non-uniform bed load sediment in alluvial rivers, Journal of Mountain Science 13 (3) (2016) 377–396.

[16] F. Exner, Über die Wechselwirkung zwischen Wasser und Geschiebe in Flüssen: Gedr. mit Unterstützg aus d. Jerome u. Margaret Stonborough-Fonds, Akademie der Wissenschaften, Wien, 1925.

[17] C. Juez, J. Murillo, P. Garcia-Navarro, Numerical assessment of bedload discharge formulations for transient flow in 1D and 2D situations, Journal of Hydroinformatics 15 (4) (2013) 1234–1257.

[18] X. Liu, A. Beljadid, A coupled numerical model for water flow, sediment transport and bed erosion, Computers & Fluids 154 (2017) 273 – 284.

[19] A. Hosseinzadeh-Tabrizi, M. Ghaeini-Hessaroeyeh, Modelling of dam failure-induced flows over movable beds considering turbulence effects, Computers & Fluids 161 (2018) 199 – 210.

[20] A. Lacasta, M. Morales-Hernández, J. Murillo, P. García-Navarro, An optimized GPU implementation of a 2D free surface simulation model on unstructured meshes, Advances in Engineering Software 78 (0) (2014) 1 – 15.

[21] B. Sanders, Integration of a shallow water model with a local time step, Journal of Hydraulic Research 46 (4) (2008) 466–475.

[22] T. Tingsanchali, C. Chinnarasri, Numerical modelling of dam failure due to flow overtopping, Hydrological Sciences Journal 46 (1) (2001) 113–130.

[23] M. Catella, E. Paris, L. Solari, 1-D morphodynamic model for natural rivers, in: River, Coastal and Estuarine Morphodynamics: Proceedings of the 4th IAHR Symposium on River, Coastal and Estuarine Morphodynamics (RCEM 2005), Urbana, Illinois, USA, 2005, pp. 283–300.

[24] K. El Kadi Abderrezzak, A. Paquier, B. Gay, One-dimensional numerical modelling of dam-break waves over movable beds: application to experimental and field cases, Environmental Fluid Mechanics 8 (2) (2008) 169–198.

[25] A. Paquier, K. El Kadi, A model for bed-load transport and morphological evolution in rivers: Description and pertinence, in: S. Benzoni-Gavage, D. Serre (Eds.), Hyperbolic Problems: Theory, Numerics, Applications, Springer Berlin Heidelberg, Berlin, Heidelberg, 2008, pp. 285–296.

[26] S. Cordier, M. Le, T. Morales de Luna, Bedload transport in shallow water models: Why splitting (may) fail, how hyperbolicity (can) help, Advances in Water Resources 34 (8) (2011) 980 – 989.

[27] J. Hudson, P. K. Sweby, Formulations for numerically approximating hyperbolic systems governing sediment transport, Journal of Scientific Computing 19 (1) (2003) 225–252.

[28] G. Rosatti, L. Fraccarollo, A well-balanced approach for flows over mobile-bed with high sediment-transport, Journal of Computational Physics 220 (1) (2006) 312 – 338.

[29] G. Garegnani, G. Rosatti, L. Bonaventura, Free surface flows over mobile bed: mathematical analysis and numerical modeling of coupled and decoupled approaches, Communications in Applied and Industrial Mathematics 2 (1).

[30] E. Fernández-Nieto, C. Lucas, T. Morales-de Luna, S. Cordier, On the influence of the thickness of the sediment moving layer in the definition of the bedload transport formula in exner systems, Computers & Fluids 91 (2014) 87 – 106.

[31] P. Gunawan, X. Lhébrard, Hydrostatic relaxation scheme for the 1d shallow water - exner equations in bedload transport, Computers & Fluids 121 (2015) 44 – 50.

[32] J. Murillo, P. Garcia-Navarro, An exner-based coupled model for two-dimensional transient flow over erodible bed, Journal of Computational Physics 229 (23) (2010) 8704–8732.

[33] X. Liu, A. Mohammadian, A. Kurganov, J. Infante-Sedano, Well-balanced central-upwind scheme for a fully coupled shallow water system modeling flows over erodible bed, Journal of Computational Physics 300 (2015) 202 – 218.

[34] J. Cunge, F. Holly, A. Verwey, Practical aspects of computational river hydraulics, Monographs and surveys in water resources engineering, Pitman Advanced Publishing Program, 1980.

[35] P. Garcia-Navarro, M. Vazquez-Cendon, On numerical treatment of the source terms in the shallow water equations, Computers & Fluids 29 (8) (2000) 951 – 979.

[36] J. Burguete, P. Garcia-Navarro, Efficient construction of high-resolution tvd conservative schemes for equations with source terms: application to shallow water flows, International Journal for Numerical Methods in fluids 37 (2) (2001) 209–248.

[37] J. Murillo, P. Garcia-Navarro, Accurate numerical modeling of 1D flow in channels with arbitrary shape. application of the energy balanced property, Journal of computational Physics 260 (2014) 222–248.

[38] G. Petaccia, L. Natale, F. Savi, M. Velickovic, Y. Zech, S. Soares-Frazão, Flood wave propagation in steep mountain rivers, Journal of Hydroinformatics 15 (1) (2013) 120–137.

[39] H. Capart, T. Eldho, S. Huang, D. Young, Y. Zech, Treatment of natural geometry in finite volume river flow computations, Journal of Hydraulic Engineering 129 (5) (2003) 385–393.

[40] J. Pitlick, R. Cress, Downstream changes in channel geometry of a large gravel bed river, Water Resources Research 38 (10) (2002) 34–1.

[41] A. Grass, Sediments Transport by Waves and Currents, Department of Civil Engineering, University College, London, UK, 1981.

[42] E. Meyer-Peter, R. Müller, Formulas for bed-load transport, in: Report on 2nd meeting on international association on hydraulic structures research, Stockholm, Sweden, 1948, pp. 39–64.

[43] G. Smart, Sediment transport formula for steep channels, Journal of Hydraulic Engineering 3 (1984) 267–276.

[44] P. Nielsen, Coastal Bottom Boundary Layers and Sediment Transport, Advanced series on ocean engineering, World Scientific, 1992.

[45] S. Khodashenas, K. El Kadi Abderrezzak, A. Paquier, Boundary shear stress in open channel flow: A comparison among six methods, Journal of Hydraulic Research 46 (5) (2008) 598–609.

[46] S. Francalanci, L. Solari, Gravitational effects on bed load transport at low shields stress: Experimental observations, Water Resources Research 43 (3) (2007) n/a–n/a.

[47] S. Ikeda, Incipient motion of sand particles on side slopes, Journal of the Hydraulics Division 108 (1) (1982) 95–114.

[48] P. Morris, D. Williams, Relative celerities of mobile bed flows with finite solids concentrations, Journal of Hydraulic Engineering 122 (6) (1996) 311–315.

[49] Z. Cao, R. Day, S. Egashira, Coupled and decoupled numerical modeling of flow and morphological evolution in alluvial rivers, Journal of Hydraulic Engineering 128 (3) (2002) 306–321.

[50] E. Savary, Y. Zech, Boundary conditions in a two-layer geomorphological model. application to a, Journal of Hydraulic Research 45 (3) (2007) 316–332.

[51] J. Murillo, P. García-Navarro, Weak solutions for partial differential equations with source terms: Application to the shallow water equations, J. Comput. Phys. 229 (11) (2010) 4327–4368.

[52] G. Rosatti, L. Begnudelli, The riemann problem for the one-dimensional, free-surface shallow water equations with a bed step: Theoretical analysis and numerical simulations, Journal of Computational Physics 229 (3) (2010) 760 – 787.

[53] A. Harten, J. Hyman, Self adjusting grid methods for one-dimensional hyperbolic conservation laws, Journal of Computational Physics 50 (2) (1983) 235 – 269.

[54] B. Spinewine, Y. Zech, Small-scale laboratory dam-break waves on movable beds, Journal of Hydraulic Research 45 (sup1) (2007) 73–86.

[55] S. Soares-Frazão, N. LeGrelle, B. Spinewine, Y. Zech, Dam-break induced morphological changes in a channel with uniform sediments: measurements by a laser-sheet imaging technique, Journal of Hydraulic Research 45 (sup1) (2007) 8795.

[56] H. Capart, B. Spinewine, D. Young, Y. Zech, G. Brooks, M. Leclerc, Y. Secretan, The 1996 lake ha! ha! breakout flood, qubec: Test data for geomorphic flood routing methods, Journal of Hydraulic Research 45 (sup1) (2007) 97–109.

[57] L. M. F., S. Y., D. S. N., B. N., L. M., Response of the Ha!Ha! River to the flood of July 1996 in the Saguenay region of Quebec: Large-scale avulsion in a glaciated valley, Water Resources Research 34 (9) (1998) 2383–2392.

[58] G. Brooks, D. Lawrence, The drainage of the lake ha!ha! reservoir and downstream geomorphic impacts along ha!ha! river, saguenay area, quebec, canada, Geomorphology 28 (1) (1999) 141 – 167.

[59] H. Capart, B. Spinewine, D. L. Young, Z. Y., G. R. Brooks, M. Leclerc, Y. Secretan, The 1996 lake ha! ha! breakout flood, qubec: Proposed test case for geomorphic flood models, in: 3rd IMPACT Workshop, Louvain-la-Neuve, Belgium, 2003.

[60] T. Mahdi, C. Marche, Prvision par modlisation numrique de la zone de risque bordant un tronon de rivire subissant une crue exceptionnelle, Canadian Journal of Civil Engineering 30 (3) (2003) 568–579.

[61] R. FERREIRA, J. LEAL, H. CARDOSO, Mathematical modeling of the morphodynamic aspects of the 1996 flood in the Ha!Ha! River, in: XXXI IAHR CONGRESS, Seoul, Korea, 2005.

[62] T.-F. Mahdi, Semi-two-dimensional numerical model for river morphological change prediction: theory and concepts, Natural Hazards 49 (3) (2009) 565–603.

[63] A. Davies, L. van Rijn, J. Damgaard, J. van de Graaff, J. Ribberink, Intercomparison of research and practical sand transport models, Coastal Engineering 46 (1) (2002) 1 – 23.

[64] L. Van Rijn, D. Walstra, M. Van Helvert, G. De Boer, Morphology of pits, channels and trenches part 1: Literature review and study approach, Tech. rep., Hydraulic Engineering Reports, Delf Hydraulics, Netherlands (2003).

Appendix A. Wave and source strengths for the augmented Roe's solver

Wave strength

Conserved variable spatial increments at each edge $i+1/2$ can be projected onto the right eigenvector base, obtaining the wave strengths $\widetilde{\alpha}_m$ at that edge:

$$\begin{aligned}
\delta\vec{U}|_{i+1/2} &= \sum_m \widetilde{\alpha}_m \widetilde{\vec{e}}_m \\
\widetilde{\alpha}_m &= \frac{\left(\widetilde{c}^2 - \widetilde{u}^2 + \prod_{k\neq m}\widetilde{\lambda}_k\right)\delta A + \left(2\widetilde{u} - \sum_{k\neq m}\widetilde{\lambda}_k\right)\delta Q + \widetilde{c}_b{}^2\delta A_s}{\widetilde{\lambda}_m\left(\widetilde{\lambda}_m - \sum_{k\neq m}\widetilde{\lambda}_k\right) + \prod_{k\neq m}\widetilde{\lambda}_k}
\end{aligned} \tag{A.1}$$

Source terms discretization

Source terms are integrated over a suitable control volume for each local Riemann problem. Then, the result is projected onto the right eigenvectors basis as a function of the Roe's average quantities at the cell edge.

$$\begin{aligned}
\widetilde{\vec{S}'}\Delta x|_{i+1/2} &= \sum_m \widetilde{\beta}_m \widetilde{\vec{e}}_m \\
\widetilde{\beta}_m &= \frac{\left(2\widetilde{u} - \sum_{k\neq m}\widetilde{\lambda}_k\right)\widetilde{S'}_2\Delta x + \widetilde{c}_b{}^2\widetilde{S'}_3\Delta x}{\widetilde{\lambda}_m\left(\widetilde{\lambda}_m - \sum_{k\neq m}\widetilde{\lambda}_k\right) + \prod_{k\neq m}\widetilde{\lambda}_k} \\
\text{with:}\quad \widetilde{\vec{S}'}\Delta x &= \begin{bmatrix} 0 \\ -g\bar{A}\left[\delta Z_R + \left(\delta\epsilon_b - \dfrac{\widetilde{c}_b{}^2}{g\bar{A}}\delta A_s\right) + \widetilde{S}_f\Delta x + \left(\delta h - \dfrac{1}{\bar{B}}\delta A\right)\right] \\ -\xi\widetilde{q}_s\ \delta B \end{bmatrix}
\end{aligned} \tag{A.2}$$

Furthermore, the value $\widetilde{q}_s$ should also balance the total solid flux at each edge, agreeing (13):

$$\begin{aligned}\xi\ \delta Q_s|_{i+1/2} &= -\widetilde{u}\widetilde{d}\ \delta A|_{i+1/2} + \widetilde{d}\ \delta Q|_{i+1/2} + \xi\widetilde{q_s}\ \delta B|_{i+1/2}\\ \widetilde{q_s} &= \frac{1}{2}A_g(u_i^3 + u_{i+1}^3)\end{aligned} \tag{A.3}$$

The friction slope $\bar{S_f}$ is evaluated as follows:

$$\widetilde{S}_f = \frac{n^2|\widetilde{u}|\widetilde{u}}{\bar{R_h}^{4/3}} \qquad \text{with:} \qquad \bar{R_h} = \frac{A_i + A_{i+1}}{P_i + P_{i+1}} \tag{A.4}$$

Appendix B. Equilibrium bed slope in rectangular channels with variable width

Considering a rectangular cross-section channel of B width and steady flow, temporal derivatives are nil and the wetted and solid discharge total derivative become:

$$\frac{dQ}{dx} = 0 \qquad \frac{dQ_s}{dx} = 0 \tag{B.1}$$

Therefore, the momentum equation reduces to:

$$\begin{aligned}\frac{d}{dx}\left(\frac{Q^2}{A} + gI_1\right) &= gA(S_0 - S_f) + gI_2\\ -\frac{Q^2}{A^2}\frac{dA}{dx} + g\frac{d}{dx}\left(B\frac{h^2}{2}\right) &= gA(S_0 - S_f) + g\frac{dB}{dx}\frac{h^2}{2}\\ -\frac{Q^2}{A^2}\left(B\frac{dh}{dx} + h\frac{dB}{dx}\right) + g\left(\frac{h^2}{2}\frac{dB}{dx} + Bh\frac{dh}{dx}\right) &= gA(S_0 - S_f) + g\frac{h^2}{2}\frac{dB}{dx}\end{aligned} \tag{B.2}$$

Reordering terms:

$$(gA - u^2B)\frac{dh}{dx} - u^2h\frac{dB}{dx} = gA(S_0 - S_f) \tag{B.3}$$

On the other hand, the total derivative of the solid discharge Q_s can be decomposed into:

$$\frac{dQ_s}{dx} = q_s\frac{dB}{dx} + B\frac{dq_s}{dx} = 0 \tag{B.4}$$

Considering a solid discharge per unit width q_s evaluated by means of the Grass model ($q_s = A_g u^3$ with $A_g = cte$) allows us to express:

$$\frac{dq_s}{dx} = 3A_g\frac{Q^2}{A^3}\frac{dQ}{dx} - 3A_g\frac{Q^3}{A^4}\frac{dA}{dx} = -3A_g\frac{Q^3}{A^4}\left(B\frac{dh}{dx} + h\frac{dB}{dx}\right) \tag{B.5}$$

Replacing (B.5) into (B.4):

$$\begin{aligned} q_s\frac{dB}{dx} - 3\frac{B}{A}A_g u^3\left(B\frac{dh}{dx} + h\frac{dB}{dx}\right) &= 0 \\ \frac{dB}{dx} - 3\frac{B^2}{A}\frac{dh}{dx} - 3\frac{Bh}{A}\frac{dB}{dx} &= 0 \\ \frac{dh}{dx} &= \frac{-2h}{3B}\frac{dB}{dx} \end{aligned} \tag{B.6}$$

Therefore, considering (B.3) and (B.6) we can express:

$$\begin{aligned} \frac{-2}{3}\frac{h}{B}(gA - u^2B)\frac{dB}{dx} - u^2h\frac{dB}{dx} &= gA(S_0 - Sf) \\ \left(\frac{-2}{3}gh^2 - \frac{1}{3}u^2h\right)\frac{dB}{dx} &= gA(S_0 - Sf) \\ \left(\frac{-2}{3}\frac{h}{B} - \frac{1}{3}\frac{h}{B}\frac{u^2}{c^2}\right)\frac{dB}{dx} &= S_0 - Sf \end{aligned} \tag{B.7}$$

Finally, one can expressed a relation between bed slope and the friction slope involving width variations as follows;

$$S_0 = \frac{-dz}{dx} = S_f - \frac{1}{3}\frac{h}{B}(Fr^2 + 2)\frac{dB}{dx} \tag{B.8}$$

being $Fr = u/c$ the Froude number.

For a prismatic rectangular cross-section channel, this expression reduced to the well-known equilibrium slope condition $S_0 = S_f$.